The Astrophysical Journal, 700:559–578, 2009 July 20 doi:10.1088/0004-637X/700/1/559

THE NATURE OF FLARE RIBBONS IN CORONAL NULL-POINT TOPOLOGY

S. Masson[1], E. Pariat[2,4], G. Aulanier[1], and C. J. Schrijver[3]
[1] LESIA, Observatoire de Paris, CNRS, UPMC, Université Paris Diderot, 5 Place Jules Janssen, 92190 Meudon, France; sophie.masson@obspm.fr
[2] Space Weather Laboratory, NASA Goddard Space Flight Center Greenbelt, MD 20771, USA
[3] Lockheed Martin Solar and Astrophysics Laboratory, 3251 Hanover Street, Palo Alto, CA 93304-1191, USA
Received 2008 December 26; accepted 2009 May 28; published 2009 July 2

ABSTRACT

Flare ribbons are commonly attributed to the low-altitude impact, along the footprints of separatrices or quasi-separatrix layers (QSLs), of particle beams accelerated through magnetic reconnection. If reconnection occurs at a three-dimensional coronal magnetic null point, the footprint of the dome-shaped fan surface would map a closed circular ribbon. This paper addresses the following issues: does the entire circular ribbon brighten simultaneously, as expected because all fan field lines pass through the null point? And since the spine separatrices are singular field lines, do spine-related ribbons look like compact kernels? What can we learn from these observations about current sheet formation and magnetic reconnection in a null-point topology? The present study addresses these questions by analyzing *Transition Region and Coronal Explorer* and *Solar and Heliospheric Observatory*/Michelson Doppler Imager observations of a confined flare presenting a circular ribbon. Using a potential field extrapolation, we linked the circular shape of the ribbon with the photospheric mapping of the fan field lines originating from a coronal null point. Observations show that the flare ribbon outlining the fan lines brightens sequentially along the counterclockwise direction and that the spine-related ribbons are elongated. Using the potential field extrapolation as initial condition, we conduct a low-β resistive magnetohydrodynamics simulation of this observed event. We drive the coronal evolution by line-tied diverging boundary motions, so as to emulate the observed photospheric flow pattern associated with some magnetic flux emergence. The numerical analysis allows us to explain several observed features of the confined flare. The vorticity induced in the fan by the prescribed motions causes the spines to tear apart along the fan. This leads to formation of a thin current sheet and induces null-point reconnection. We also find that the null point and its associated topological structure is embedded within QSLs, already present in the asymmetric potential field configuration. We find that the QSL footprints correspond to the observed elongated spine ribbons. Finally, we observe that before and after reconnecting at the null point, all field lines undergo slipping and slip-running reconnection within the QSLs. Field lines, and therefore particle impacts, slip or slip-run according to their distance from the spine, in directions and over distances that are compatible with the observed dynamics of the ribbons.

Key words: methods: numerical – MHD – Sun: corona – Sun: flares – Sun: magnetic fields – Sun: UV radiation

Online-only material: mpeg animations

1. INTRODUCTION

Ribbons observed in Hα and in the ultraviolet (UV) wavelengths are among the most obvious signature of solar flares. They correspond to the chromospheric footpoints of coronal loops that have reconnected (Sturrock 1968). Accelerated particles, flowing down from the reconnection site along the reconnected magnetic field line generate ribbon-shaped brightenings in the denser lower portion of the solar atmosphere (Priest & Forbes 2002) and can be observed from the hard X-ray (HXR) range to the visible wavelength. Ribbons thus provide a significant amount of information about the connectivity and the topology of the magnetic field lines involved in the reconnection process (Gorbachev et al. 1988; Gorbachev & Somov 1989).

Ribbons are commonly associated with some very specific field lines of the magnetic configuration, the separatrices, which divide the total volume in domains of distinct magnetic connectivity. Separatrices are preferential sites for the formation and building-up of intense current layers (e.g., Lau & Finn 1990; Priest & Titov 1996) and thus particles are likely to be accelerated along these specific locations where reconnection occurs. Observations show that indeed ribbons are located at the intersection of the separatrices with the lower atmosphere (Mandrini et al. 1991, 1995; Démoulin et al. 1994b; van Driel-Gesztelyi et al. 1994). In four-ribbon flares, typical of confined flare, the four locations of enhanced emission map the four intersection of the solar chromosphere with the separatrices originating from the reconnection site. Similarly, in the case of the classical two-ribbon flares, generally associated with solar eruption, the two ribbons correspond to footpoints of the two separatrices separating closed and open-field regions.

But a two-ribbon flare does not necessarily imply a solar eruption. Ribbons are also sometimes associated with quasi-separatrix layers (QSLs; Démoulin et al. 1997; Mandrini et al. 1997). There are two reconnection regimes in the continuous reconnection in QSLs. An apparent slippage velocity of reconnecting field lines which is sub-Alfvénic implies slipping reconnection, whereas a super-Alfvénic slippage velocity defines the slip-running reconnection (Aulanier et al. 2006). Depending on the magnetic configuration, reconnection in QSLs can result in the formation of only two ribbons without necessarily involving the opening of magnetic field lines (Démoulin et al. 1997).

Magnetic null points are typical structures generating separatrices. Null points are common features in the solar atmosphere (Schrijver & Title 2002) and many flares have been associated

[4] College of Science, George Mason University, Fairfax, VA 22030, USA.

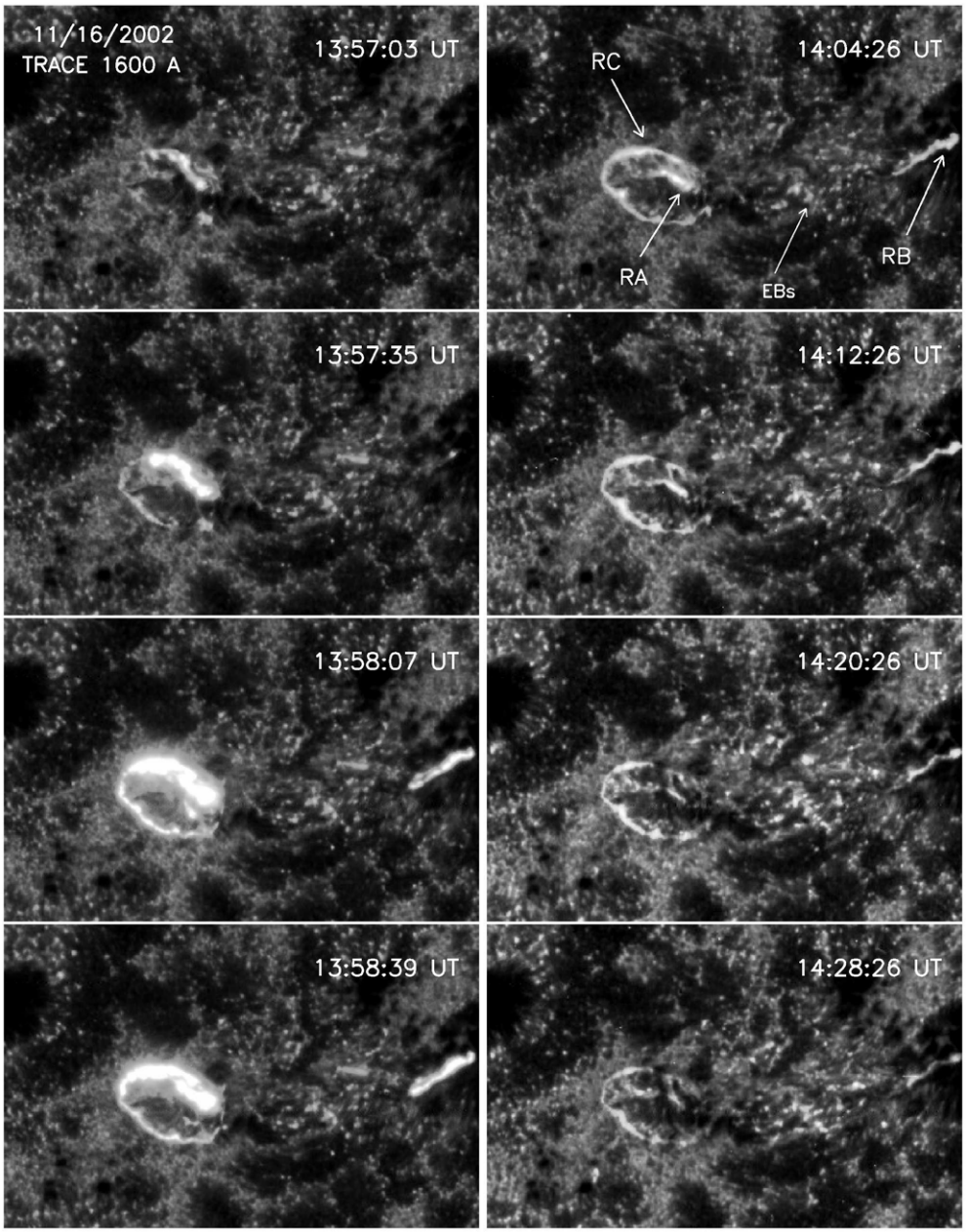

Figure 1. *TRACE* observations in the 1600 Å bandpass of the peak phase of the C-class flare occurring in AR 10191 on 2002 November 16. The left column shows the impulsive phase of the flare whereas the right column shows the decaying phase of the flare. The FOV is $192'' \times 192'' = 141$ Mm $\times$ 141 Mm. The time interval between each *TRACE* image is of 8 minutes in the right column and 32 s in the left one. Upper right panel: RA, RB, and RC denote three different flare ribbons, as described in the text, and EBs indicate the UV counterparts of the Ellerman bombs in the emerging flux region. The mpeg animation has a 3s cadence between 13:56 UT and 14:03 UT, and a 9s cadence otherwise.

(An mpeg animation of this figure is available in the online journal.)

with such topology (e.g., Démoulin et al. 1994a; Mandrini et al. 1995; Fletcher et al. 2001). In addition, evidences of the presence of magnetic null points have also been found in several eruptive events (e.g., Aulanier et al. 2000; Manoharan & Kundu 2003). Magnetic field lines going through a three-dimensional null point are of two types (Parnell et al. 1996; Lau & Finn 1990; Longcope 2005): the majority of them forms a surface, the fan of the null. The fan surface divides the volume into two regions having a distinct connectivity, generating a two flux system. From the null also originate two singular field lines, the two spines, each of them belonging to one connectivity domain (compare Figure 1 of Pariat et al. 2009). In the matrix determined by the Taylor expansion of the magnetic field in the vicinity of the null, the fan is formed by the eigenvectors of the two like-sign eigenvalues while the spine correspond to the third eigenvector (Parnell et al. 1996).

These separatrix field lines define preferential sites for the formation of current sheets and thus for magnetic reconnection. Priest & Titov (1996) defined *spine reconnection* and *fan reconnection* respectively when field lines flip from one spine to the other and when they flip around one particular spine along the fan. Pontin et al. (2004, 2005) have analytically studied the occurrence of these reconnections in three dimensional depending on whether electric currents primarily develop along the fan surface or the spine field lines. Several numerical simulations (e.g., Rickard & Titov 1996; Galsgaard & Nordlund

1997; Galsgaard et al. 2003; Pontin & Galsgaard 2007; Pontin et al. 2007a; Pariat et al. 2009) have studied how reconnection can occur in single three-dimensional null points. Pontin & Galsgaard (2007) have in particular studied the development of current sheets when the spines or the fan are disturbed by rotational or shearing perturbations away from the null. They showed that shearing motions are more likely to form intense currents localized at the null point itself while rotations of the spines (resp. the fan) tend to generate current sheets more extended along the fan (resp. the spines). In Pontin et al. (2007a), they extended the study of the build-up of a current sheet at the null when the spines are sheared by boundary-driven motions. They demonstrated that the induced shearing motion induces a modification of the null structure: the ratio of the eigenvalues of the null point evolves, i.e., the angle between the spine and the fan surface diminishes. When plotting field lines around the spines, it appears that the spines do not seem to be co-aligned (see Figure 6 in Pontin et al. 2007a) as if the two spines had slid apart along the fan surface. The current sheet is particularly important along the line that joins the two spines. As predicted by Antiochos (1996), this shear of the spine is particularly important to explain the build-up of a thin sheet of intense electric currents and to understand how efficient reconnection occurs in a single three-dimensional null-point topology. The effect of the nonlinear reconnection is to attempt to bring the two spines back into alignment (Antiochos et al. 2002). In Pariat et al. (2009), a very impulsive and brutal shear of the spines along the fan surface had also been forced which led to a tremendous amount of reconnection.

But what can observations teach us about the particular behavior of reconnection in a single ideal three-dimensional null point? First, what would be the shape of the ribbons if reconnections occurred in a topology involving such a single null point? In a closed field region having a single null point, the intersection of the fan with the boundary, should be a closed curve more or less circular depending on the axisymmetric properties of the magnetic field distribution. When reconnection occurs, ideally, one can also foresee that a quasi-circular ribbon corresponding to the intersection of the fan surface with the chromosphere should be observed. In addition, two point like kernels (one located within the ribbon circle and the other outside) tracing the footpoints of the inner and outer singular spine field lines should a priori simultaneously appear. Are such events frequently observed?

The literature describing such circular/ellipsoidal ribbons is surprisingly small. The first reason is that null-point reconnection in the closed field region may not be very common. In most observed cases, either several null points are present in the corona, the reconnection occurring along the separators linking couples of null points, leading to the classical parallel two ribbons flares, or reconnection occurs along separatrices related to bald patches (Titov et al. 1993) or due to QSLs. Another possibility is that, even when a single null point is present, one direction is privileged in the fan because one of its eigenvectors has larger amplitude than the other, along which magnetic flux concentrates in the vicinity of the null. The mapping of the fan on the photosphere could thus be an ellipsoid-like curve with a very significant eccentricity and the corresponding ribbon would appear very linear.

However, some circular-ribbon events do exist. A clear published example is the flare of 2001 December 13, in the active region AR 9733 (Ugarte-Urra et al. 2007). There the ribbon presents a circular shape which exactly matches the footpoints of the fan field lines extrapolated in the potential field approximation. In the present paper, we thoroughly study the AR 10191 and the C-class flare of 2002 November 16, observed in the UV continuum by the *Transition Region and Coronal Explorer* (*TRACE*; Handy et al. 1999), during which a circular ribbon is also present (Section 2). From magnetograms acquired with the *Solar and Heliospheric Observatory* /Michelson Doppler Imager (*SOHO*/MDI; Scherrer et al. 1995), we perform a potential field extrapolation which demonstrates that this circular ribbon indeed corresponds to the intersection of the lower layer of the solar atmosphere with the fan field lines originating from a coronal null point (Section 3).

The null-point topology having being confirmed, what can we learn from the ribbon evolution about null-point reconnection? All the fan field lines going through the null point where the current sheet is formed, the ribbon should a priori be illuminated simultaneously all along. Nonetheless we observe that the brightenings occur progressively along the fan separatrix. What does it imply on the reconnection mode? Which of *fan reconnection*, *spine reconnection* or *sheared-spine reconnection* is favored? Which field lines are effectively reconnecting? When are they reconnecting, and in which order? Another set of intriguing questions are related to the elongated ribbons observed at the footpoint of the spine. Why do not they appear as spatially localized kernels? What does it imply about the dynamic of the null-point reconnection?

In order to bring some answers to these questions and to understand more deeply the mechanisms that lead to the formation of the ribbons, we performed a magnetohydrodynamics (MHD) numerical simulation, using the observed magnetogram and the extrapolation as the initial configuration. Note that this simulation of a flaring event is one of the first to use observed magnetograms as realistic initial and boundary conditions. The numerical model is described in Section 4 and the results of this simulation are presented in Sections 5–7.

2. THE C-CLASS FLARE ON 2002 NOVEMBER 16

2.1. UV Ribbons

The C-class flare that occurred on 2002 November 16 within AR 10191 was observed with the *TRACE* spacecraft in the 1600 Å UV continuum. The spatial and temporal resolution of the observations are respectively of 0.″5 and of 3.2 s. Figure 1 (as well as the movie available in the electronic version) presents the temporal evolution of the flare, during which three ribbons can be distinguished. A quasi-circular ribbon (noted RC in Figure 1) encloses an elongated ribbon, RA, while third elongated ribbon, RB, is located outside the circular ribbon RC.

Before the triggering of the main flare, some faint brightenings appear on the north–west part of the ribbon RC at 13:11:14 UT. Although these brightenings evolve (see the movie), their intensity and their displacement remain weak until the start of the main flare at 13:57:03 UT. Between 13:14 UT and 13:18 UT some bright transients develop (east of RC brightenings) and seem to form intermittent loops (see the UV movie in the electronic version). These UV emissions could be identified as a precursor of the flare, during which the reconnection rate would not lead to a substantial flux transfer across the separatrices.

During the main flare, we can identify two phases of the evolution of the ribbons. The first phase, starting at 13:57:03 UT (left column of Figure 1) corresponds to the impulsive phase of the flare. At 13:57:03 UT, several fragments of RC start

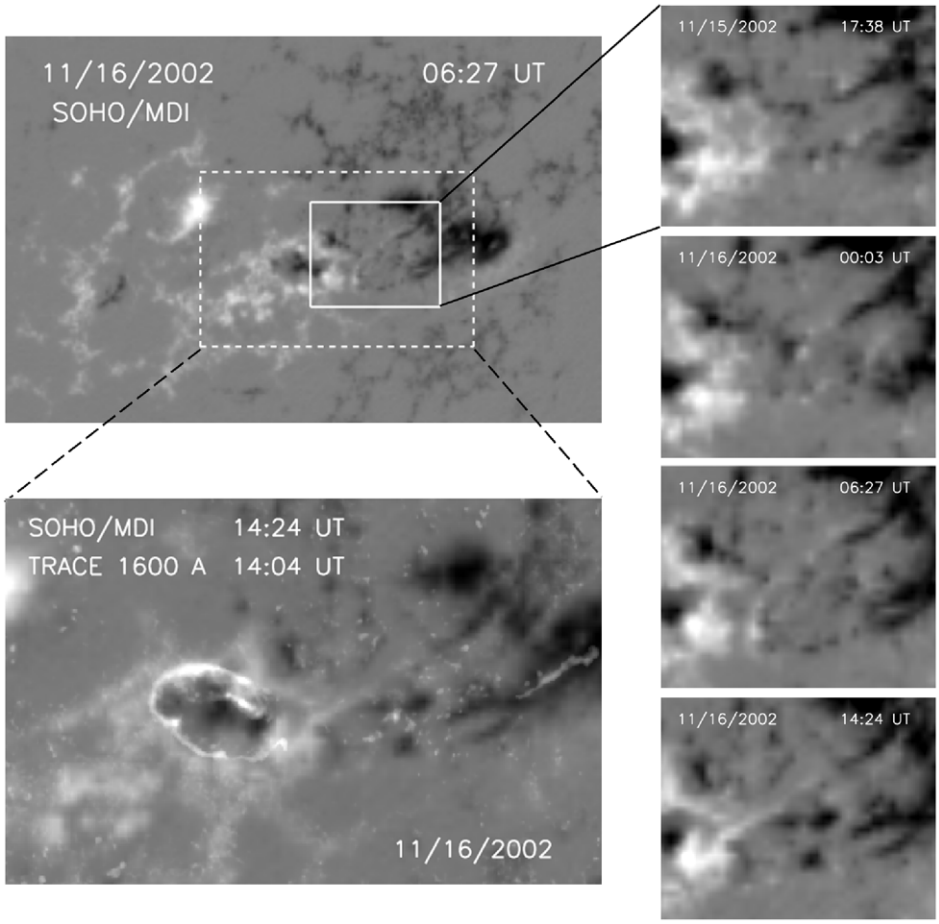

Figure 2. *SOHO*/MDI observations of AR 10191 prior to the C class flare. Upper left panel: the longitudinal magnetogram by MDI. The FOV is $396'' \times 257'' = 291$ Mm $\times$ 189 Mm. Bottom left panel: *TRACE* observation at 1600 Å co-aligned with and overlaid on the photospheric magnetogram used for the extrapolation, in the FOV indicated by the dashed white rectangle on the upper left panel. Right column: time series of MDI magnetograms showing the evolution of emerging flux event. The FOV of these images is indicated by the solid white rectangle in the top left panel.

to brighten simultaneously, distributed along an ellipsoidal shape. The emission from the north part of RC increases and eventually starts to saturate the detector at 13:57:32 UT. This brightening actually corresponds to the junction of the north part of the ribbon RC with the ribbon RA: both appear as a single structure during this phase of the flare. At that time, far west of RA/RC, a bright kernel appears on the edge of the leading sunspot, latter forming the elongated ribbon RB. It is worth noting that the formation of RB is delayed by $\sim$30 s compared to the time of the first observed emission originating from RA and RC. After 13:57:32 UT, all the ribbons quickly expand to their maximum elongation, while the global intensity of their emission increases and concomitantly peaks around 13:58:39 UT. The spreading of the brightenings along the ribbon direction is a well-known phenomenon in the initial stage of the flare (e.g., Moore et al. 2001; Fletcher et al. 2004). Between 13:57:35 UT and 13:58:07 UT, the brightening along RB spreads simultaneously eastward and westward whereas along RC an overall counterclockwise pattern is observed. The arc of saturated emission along RC extends significantly eastward while no similar feature is observed westward. A similar counterclockwise spreading of the emission is also observed in the south–west section of the ribbon RC.

The second phase, after 14:04:26 UT, corresponds to the decay phase of the flare. RC and RA can here be clearly discriminated. The intensity of the emission decreases. The east portion of RA is the first to disappear and the decrease seems to propagate westward. Along RC, the emission weakens counterclockwise from the top right of the ribbon. The intensity of RB progressively decreases toward the west. Overall, the evolution of the brightenings in each ribbon seems to follow the same pattern during the impulsive and the decaying phases.

In addition to the ribbon flare, numerous brief small localized brightenings can be observed in the inter-spot region, between RB and RA/RC (they can be more clearly identified with the movie available with the electronic version). These brightenings seem to be relatively unaffected by the ribbon flare: neither their distribution nor their evolution present noticeable changes during the flare. These brightenings are likely to be associated with Ellerman bombs (e.g., Georgoulis et al. 2002; Pariat et al. 2007) and are indicated as Ellerman Bombs (EBs) in Figure 1.

As presented in Section 1, the presence of a quasi-circular ribbon may be a good indicator of the presence of a null point. But only a topological study, using an extrapolation of the magnetic field above the photosphere, can really confirm the existence of such null point.

2.2. Flux Emergence

So as to determine the magnetic topology of the AR 10191, we used full-disc MDI photospheric magnetograms, which time cadence is 96 minutes and pixel size is $1''.977$. Longitudinal

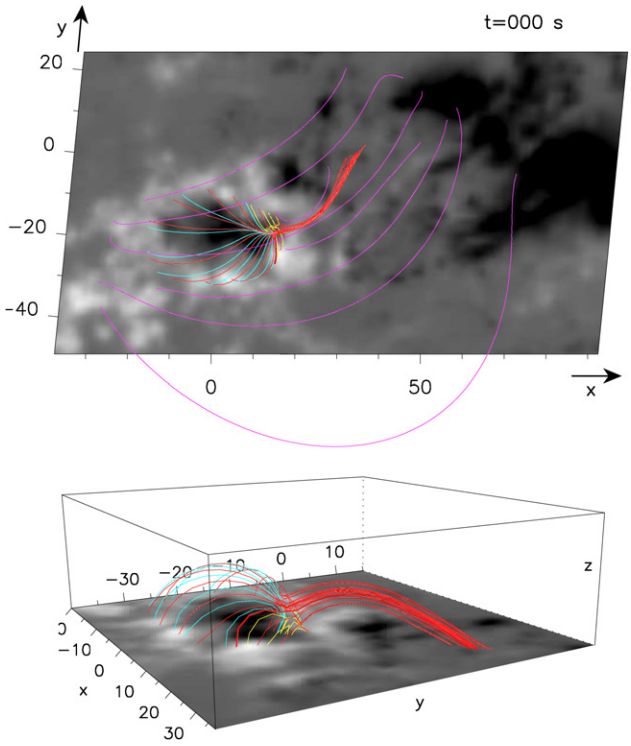

Figure 3. Result of the potential field extrapolation of AR 10191, emphasizing the null-point topology. Top panel: line-of-sight view. Bottom panel: a side view of field lines passing close to the three-dimensional null point. Spatial units are in Mm; the plotted domain is such as $x \in [-20, 38]$, $y \in [-40, 15]$, and $z \in [0, 18]$. In both panels, the same field lines are plotted over a longitudinal magnetogram: the yellow, red, and blue field lines passing close to the three-dimensional null point materialize the spine-fan topology, whereas the pink field lines represent the main bipolar magnetic field of the AR (see Section 3.1).

magnetograms of the AR 10191 are presented in Figure 2, at different times before and during the C-class flare. The field of view (FOV) is equal to 291 Mm × 189 Mm. The top-left panel of Figure 2 presents the active region several hours before the onset of the flare. The AR is formed of a negative leading-sunspot and a positive trailing-sunspot. Within the trailing positive region, we remark the presence of a circular area of negative polarity (hereafter this polarity will be called "parasitic polarity"). The flux in this parasitic polarity increased during the days preceding the flare and cospatial pores could be observed in white light.

Between November 15, 17:38 UT and November 16, 06:27 UT, an important flux emergence occurred in the central region of the AR, between the main polarities (Figure 2, within the white rectangle). The evolution of the magnetic field shows the apparition of several dipoles and the diverging migration of opposite-sign polarities, typical for emerging flux events (Schmieder & Pariat 2007). Ellerman bombs, observed in UV in the center of this flux emergence region (see Section 2.1), are also typical features of emerging flux regions (Pariat et al. 2004). In Figure 2, we also observe that the magnetic flux distribution adopts a horseshoe pattern composed with ribbon-like concentrations of positive polarities in the north and negative polarities in the south. We noted as well the merging with the main positive polarity of several patches of positive flux which had previously emerged at the west of the parasitic polarity.

Significant flux emergence occurring within an active region is usually a strong precursor of a flare activity (e.g., Schrijver et al. 2005; Schrijver 2009). Along with the flux emergence, magnetic energy has been injected in the active region, generating nonpotential field within the active region. The emerging flux is likely to have interacted with the pre-existing field, eventually destabilizing the magnetic configuration, resulting in the release of free energy through magnetic reconnection (following the classical model of Heyvaerts et al. 1977).

The co-alignment of the *TRACE* 1600 Å image at 14:04 UT and the MDI magnetogram at 14:24 UT (see Figure 2, bottom left panel) has been done manually. We rebinned the MDI magnetogram to the pixel size of the *TRACE* image, and we overlaid these two images using faculae and sunspots. Details of this co-alignment method are described precisely in Aulanier et al. (2000). We first remark that the UV bright points are located in this emerging flux region and that they tend to be located along the polarity inversion line. This agrees well with the hypothesis that these UV bright points are the transition region signature of Ellerman bombs (Pariat et al. 2007). In addition, we observe that the quasi-circular ribbon RC encircles the large area of the negative flux within the positive trailing spot. This ribbon is located around the polarity inversion line of this large parasitic negative polarity. This is coherent with the idea that the ribbon RC corresponds to the photospheric footprint of the fan surface generated by a magnetic null point.

3. INITIAL FIELD CONFIGURATION AND MHD MODEL

3.1. Potential Field Extrapolation

To perform the extrapolation, we used the MDI magnetogram from November 16, 06:27 UT (a few hours before the flare) as the bottom boundary condition for the vertical magnetic field $b_z(z = 0)$. We considered the potential field approximation (i.e., $\nabla \times \mathbf{b} = 0$), not only because it simplifies the computation without qualitatively modifying the magnetic field topology (which we checked by also calculating linear force-free fields with $\nabla \times \mathbf{b} = \alpha \mathbf{b}$, with $\alpha = \mathrm{cst}$) but also because it results in a configuration which has zero free magnetic energy (compare Section 4.1). The extrapolation was done using the fast Fourier transform method (Alissandrakis 1981). In order to avoid the aliasing artifacts due to the periodic side-boundary conditions, we enclosed the observed magnetogram, which FOV is equal to 291 Mm × 189 Mm (the same as in Figure 2), in a larger domain of $b_z(z = 0)$. Thereby, the domain considered for the extrapolation was a box of 600 Mm × 600 Mm and the extrapolation was performed over 1024 modes.

The extrapolation indeed confirms that a single null point is present above the photospheric boundary, above the western side of the parasitic polarity. Iterative interpolations locate the null point at a height of 1.5 Mm. This null point divides the coronal volume in two connectivity domains, separated by the fan surface. In each domain a spine is present, which we refer to the inner (resp. outer) spine for the one confined below (resp. emerging away from) the fan surface (as in Figure 1 of Pariat et al. 2009). The two eigenvectors defining the fan are respectively orientated almost perfectly along the north–south and the east–west directions. The north–south eigenvectors has a larger amplitude, by a factor of ∼8, than the other one. This induces an asymmetry in the fan.

Figure 3 shows the result of the extrapolation and the topology of the AR (note that the FOV of Figure 3 is smaller than the domain used for the extrapolation). The pink field lines belong to the outer connectivity domain and represent the magnetic field associated with the large scale main bipolar magnetic field of the AR. The blue, yellow, and red field lines are passing close to the null point and thus materialize the fan-spine topology.

The red field lines belong to the outer connectivity domain. They materialize the outer spine, anchored in the leading negative magnetic sunspot, and the outer surface of the fan. The intersection of the fan surface with the photosphere as a quasi-circular shape which encloses completely the parasitic negative polarity of the trailing sunspot. The blue and yellow field lines belong to the inner connectivity domain. They connect the parasitic negative polarity with the positive surrounding polarity. They materialize the inner regions below the fan surface and also trace the location of the inner spine.

3.2. Preliminary Interpretation and Puzzles

Comparing the positions of the ribbon RC and the magnetic topology, we remark that RC is almost perfectly cospatial with the intersection of the fan surface with the photosphere. They both assume the exact same quasi-circular-like shape. This agrees very well with the flare models which stipulate that ribbons are to be found at the footpoints of the separatrices (see references in Section 1). This spatial correspondence between the magnetic configuration and the pattern of the flare is consistent with a null-point reconnection. Null points are preferential sites for a current sheet to form and for reconnection to occur (e.g., Priest & Titov 1996; Pontin et al. 2007a). The brightenings observed by *TRACE* are due to the interaction with the transition region and the chromosphere of energetic particles accelerated at the reconnection site and moving along the field lines reconnecting across the separatrices. When reconnection occurs at a single three-dimensional null-point, since every fan and spine field lines pass through the null, emissions are expected to originate from all their footpoints. We indeed observe that during the impulsive phase, RC brightens over the entire mapping of the fan at the photosphere, which is fully consistent with three-dimensional null-point reconnection. The asymmetry of the eigenvectors of the fan (compare Section 3.1) can partly explain the fact that most of the emission originates from the north part of RC, since it corresponds to the direction of the largest eigenvalue, along which most of the reconnected field lines form. In addition, the specific distribution of the nonpotential magnetic flux within the inner domain should also account for a large part of the asymmetry of the emission. However, this cannot be fully modeled by our potential extrapolation.

Similarly, the ribbons RA and RB should respectively correspond to the inner and the outer spine. The agreement between RA and the extrapolated inner spine is indeed good. Nonetheless RB is not co-spatial with the position of the footpoint of the outer spine: the footpoint of our outer spine is located in the middle of the emerging flux region, whereas RB is located in the penumbra of the leading spot. This discrepancy may be due to a bias of our magnetic field extrapolation. Between the time at which the extrapolation has been performed and the time of the flare, a slow diverging motion due to the flux emergence had occurred for several days, which separated the main polarities of the AR. It is therefore possible that the "real" outer spine had been advected away from the center of the magnetic flux emergence region over the previous days. As a result, the real magnetic field in the active region is certainly nonpotential and rather in a nonlinear force-free state. While the potential field hypothesis predicts correctly the existence of the topological structures (the null point, the fan, the spines), it probably fails in quantifying perfectly the location of the footpoint of the outer spine. However, due to the overall very good agreement of RA and RC with the two other topological structures, it is very likely that RB also maps the location of the outer spine in the real magnetic field.

Nevertheless, the dynamical behavior of the observed ribbons cannot be fully understood solely with this topological study. The counterclockwise pattern of the emission in RC is a puzzling feature of the flare evolution since one would expect simultaneous brightening over RC. In addition, the fact that the ribbon RB appears a relatively long time after the first emission originating from the ribbon RC is incompatible with the fact that fan and spine footpoints should simultaneously brighten during null-point reconnection. Furthermore, since the spines are both singular field lines, one would expect that the emission occurring at their intersection with the denser layer of the solar atmosphere would be if not point-like, at least rather-circular and of a relatively small size. However, we observe that RA and RB (which are the transition region emissions associated with the spines) progressively grow during the flare and assume the shape of elongated ribbons (compare Section 2.1).

A classical explanation is that, as reconnection proceeds, the location of the reconnection site moves. As line-tied field lines reconnect, they change the connectivity domain. This transfer of flux may induce a relative growth of some connectivity domains relatively to others. Since the separatrix surfaces are defined as the boundary between the different connectivity domains, the relative size variation of the different domains during reconnection induces not only the displacement of the separatrix surface together, but also with the reconnection site. Standard models of solar eruption call on this process to explain the separation of the two ribbons (e.g., Priest & Forbes 2002). These displacements are thus not caused by plasma motion but by the continuous injection of an energy flux into newly connected field lines (Pneuman 1981; Schmieder et al. 1987; Lin 2004). The change of location of the reconnection site also allows us to interpret the motion of the HXR footpoint emissions whether they are separating, or having parallel or anti-parallel motions (e.g., Krucker et al. 2003; Grigis & Benz 2005; Bogachev et al. 2005).

Similarly, with the null-point reconnection presently studied, does the location of the topological structures evolve along with the position of the null? Can the elongation of the spine ribbons be interpreted by the displacement of the spine? Does the elongation of the ribbons map the evolution of the spine-footpoint locations? In order to address these questions, we performed a MHD numerical simulation modeling the evolution of the magnetic configuration. We wish to determine if throughout the prescribed evolution of the magnetic field, we can generate motions of the separatrices field lines that would be able to account for the extended ribbons, as predicted by the classical models of flare.

4. NUMERICAL MODEL

We perform a three-dimensional numerical simulation so as to reproduce as reliably as possible the AR and the flare observed evolutions. We use the potential field calculated in Section 3.1 to set the initial magnetic configuration. Assuming that the emerging flux is at the origin of the flare, we drive the system by line-tied boundary motions reproducing the observed separation of the photospheric magnetic flux concentrations. The numerical model is described in Section 4.1 and the applied boundary motion is presented in Section 4.2.

4.1. Equation and Boundary Conditions

We use the explicit three-dimensional MHD code described in Aulanier et al. (2005a), to which we add finite-β adiabatic effects. The numerical simulation is performed in a Cartesian domain in which x and y are the horizontal axes and z is the vertical axis. The computational domain is a subset of the extrapolation one. Along the horizontal coordinates, it is centered at the null point and covers the volume defined by $x \in [-37.4, 92.5]$ Mm, $y \in [-49, 24.4]$ Mm, and $z \in [0, 60]$ Mm. This domain is the one displayed in Figure 3. The mesh is nonuniform with $237 \times 201 \times 201$ grid points. The grid space evolves as a geometric series in all directions. Horizontally in x and y, the smallest cell is centered around the null point; the reason of the geometric series is equal to $R_{x,y} = 1.03$; the smallest size of the mesh is $d^{x,y}_{\min} = 0.06$ Mm and the largest one, at the corners of the (x, y) domain, reaches $d^{x}_{\max} = 2.4$ Mm and $d^{y}_{\max} = 1.3$ Mm. Along z, the reason is $R_z = 1.016$, and the smallest and largest cells are respectively of $d^{z}_{\min} = 0.04$ Mm and $d^{z}_{\max} = 2$ Mm.

Our calculation solves the following set of equations using a high-order finite-difference and predictor–corrector scheme:

$$\frac{\partial \rho}{\partial t} = -\nabla \cdot (\rho \mathbf{u}) + \kappa \triangle \rho \,, \tag{1}$$

$$\frac{\partial T}{\partial t} = -(\mathbf{u} \cdot \nabla) T - (\gamma - 1) T (\nabla \cdot \mathbf{u}) + \kappa \triangle T \,, \tag{2}$$

$$\frac{\partial \mathbf{u}}{\partial t} = -(\mathbf{u} \cdot \nabla)\mathbf{u} - \frac{k_B}{m_P}\left(\nabla T + \frac{T}{\rho}\nabla \rho\right) + (\mu\rho)^{-1}(\nabla \times \mathbf{b}) \times \mathbf{b} + \nu \triangle' \mathbf{u} \,, \tag{3}$$

$$\frac{\partial \mathbf{b}}{\partial t} = \nabla \times (\mathbf{u} \times \mathbf{b}) + \eta \triangle \mathbf{b} \,, \tag{4}$$

where ρ being the mass density, T the plasma temperature, $\mathbf{u}$ the plasma velocity, and $\mathbf{b}$ the magnetic field. The constants γ, k_B, m_P, and μ are respectively the ratio of the specific heat chosen here at 5/3, the Boltzmann constant, the proton mass, and the magnetic permeability. All these equations are actually written in the code in their fully developed form. The magnetic force is expressed in the Lorentz form in Equation (3) in order to properly treat singular behavior at the null point where the Alfvén speed, c_A, becomes zero. Under this form, a fast-mode wave can be converted into an acoustic mode around the null when it reaches the $\beta \simeq 1$ shell. This prevents the null-point structure to evolve via the diffusive terms only.

The operators $\nu \triangle' \mathbf{u}$ and $\eta \triangle \mathbf{b}$ correspond respectively to a viscous filter that uses a pseudo-Laplacian adapted to the local mesh (see Aulanier et al. 2005a, for more details), and a standard collisional uniform resistive term. $\kappa \triangle \rho$ and $\kappa \triangle T$ are a nonphysical explicit diffusive terms which smooth the gradients of density and temperature, and which help to stabilize the numerical computation. The diffusion coefficients are taken to be equal to $\eta = 1.2 \times 10^8$ m^2 s^{-1} and $\kappa = 12 \times 10^8$ m^2 s^{-1}, thus leading to characteristic diffusive speeds of $u_\eta = 3$ km s^{-1} and $u_\kappa = 30$ km s^{-1} at the scale of the smallest mesh interval ($\sim$40 km). We use a strong viscous coefficient that results in a characteristic velocity diffusion speed of $u_\nu = 150$ km s^{-1} that does not vary with the local mesh size. The small value of η allows a nearly ideal treatment of the corona out of narrow current sheets. We have chosen probably unnecessary large values for the other coefficients, so as to broaden the narrow vortical layers that develop around the null point during the calculation by more than five grid points, so as to ensure numerical stability.

For the top and side faces of the domain, we prescribe open boundary conditions. At the bottom boundary, in order to account for the photospheric magnetic driving of the corona, we use line-tied and reflective conditions. The evolutions of the vertical magnetic field and of the flow fields at bottom boundary are therefore completely prescribed, and not affected by the evolution within the computational domain (see Grappin et al. 2008, for a discussion of the validity of the line-tied approximation). The forcing motions are described in Section 4.2.

As an initial condition for the magnetic field we used the output of the magnetic field extrapolation performed in Section 3.1. The uniform extrapolation mesh along x and y being different from the one used in the numerical simulation, we interpolated the results of the extrapolation using trilinear interpolation on the numerical nonuniform mesh. This leads to residual Lorentz forces whose stress is quickly carried away from the domain through the open boundaries in the form of magneto-acoustic waves.

In this simulation, we neglect the gravitational effect and prescribe an initial uniform atmosphere. Initially, the uniform density is given by $\rho = b^2_{\max}/\mu c^2_{A,\max}$, where we chose the maximum of the Alfvén speed to be $c_{A,\max} = 1000$ km s^{-1}, that is located where the magnetic field is the strongest, on the right-top of the FOV of the magnetogram presented on the top left panel of Figure 3. The resulting initial particle density $n \simeq 6.8 \times 10^{12}$ cm^{-3} is more typical of the chromosphere, but choosing coronal values lower by $\sim$4 orders of magnitude would have required about $\sim$100 times more computational time to perform the same simulations, all things being equal. This results in local coronal Alfvén speeds above the emerging flux region and above the parasitic polarity of $c_{A,l} \sim 200$–400 km s^{-1}. The initial temperature is assumed to be uniform and equal to $T = 3 \times 10^5$ K, resulting in a sound speed $c_S \simeq 64$ km s^{-1}. Even though this temperature is typically 10 times lower than in the corona, its choice was motivated to obtain the best compromise to maintain an early subsonic quasi-static coronal evolution together with $\beta \ll 1$ everywhere in the low corona (except close to the null point).

Such nonsolar atmospheric parameters are actually typical of most finite-β multidimensional MHD simulations of the solar corona which make use of realistic magnetic field amplitudes, when one rescales them into physical units. Still those simulations, including the present one, are calculated in physical regimes that tend to those of the quasi-static, magnetically dominated and highly conductive solar corona, as characterized by the following MHD dimensionless numbers: the Mach numbers of our prescribed photospheric driving (see Section 4.2) are $M_A = u_D/c_{A,l} \sim 0.05 - 0.1 \ll 1$ and $M = u_D/c_S \sim 0.3 \leqslant 1$; our local plasma $\beta = (2/\gamma)(c_S/c_{A,l})^2 \sim 0.03$–$0.12 \ll 1$ (we get $\beta \leqslant 1$ only within a sphere of about 1 Mm radius around the null point, and at high altitudes $z \geqslant 35$ Mm); our Reynolds and Lundqvist numbers at the typical length scale $L = 60$ Mm (characterized by the sizes of the null-point separatrix and that of the emerging flux area) are $Rm = u_D L/\eta = 10^4 \gg 1$ and $Lu = c_{A,l} L/\eta \sim 1 \times 10^5 - 2 \times 10^5 \gg 1$.

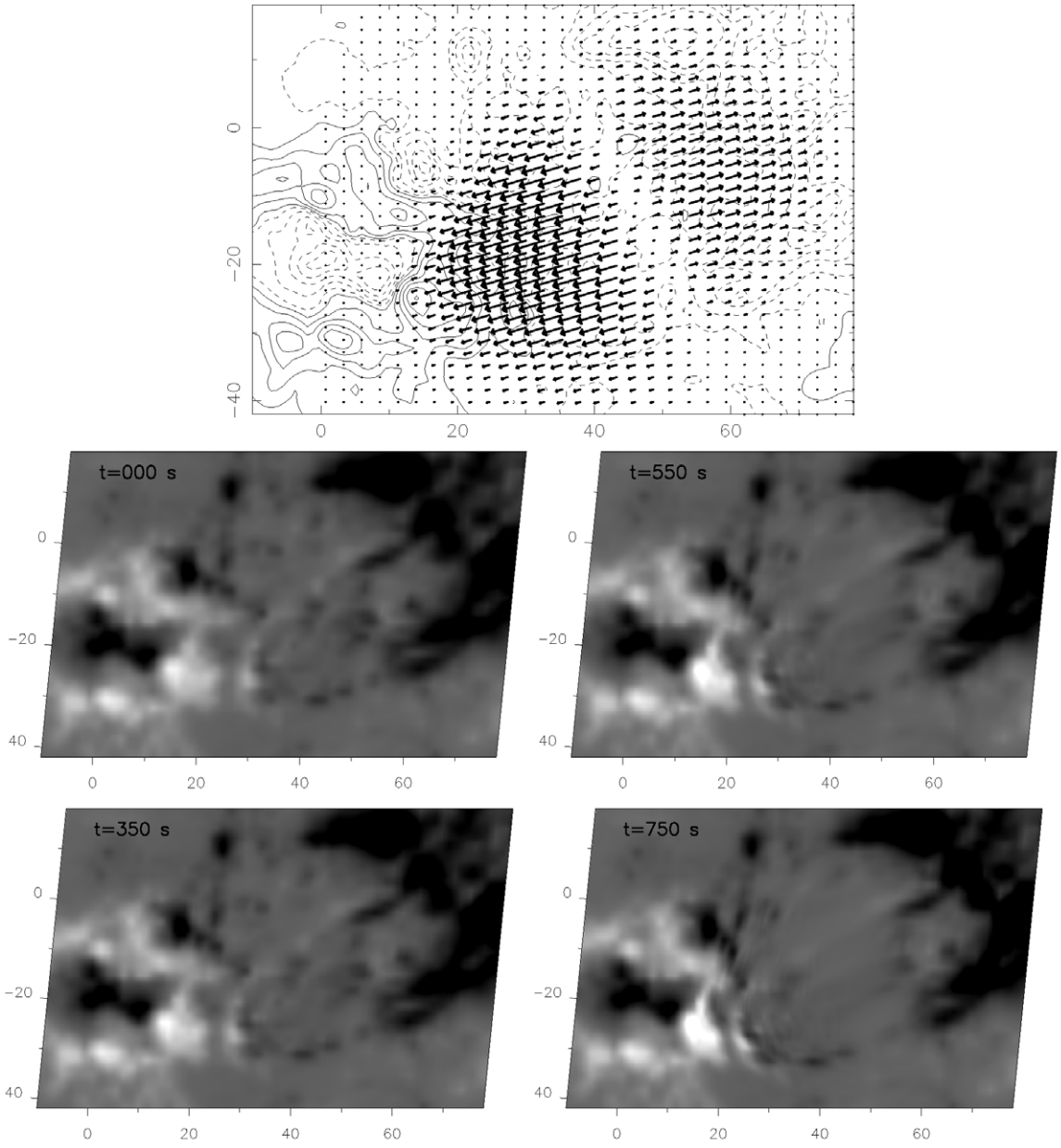

Figure 4. Top panel: photospheric flow pattern prescribed in the MHD simulation, so as to mimic the observed diverging motions in the flux emergence area (see Figure 2). Bottom panels: evolution of the photospheric vertical field $b_z(z = 0)$ during the simulation. Spatial units are in Mm.

4.2. Bottom Boundary Driving

As described in Section 2.2, a flux emergence has occurred in the inter-spot region before the onset of the flare. We assume that this flux emergence is the driver of the flare. So as to simulate the evolution of the active region, we constrain the magnetic configuration by emulating this flux emergence event using an analytical divergent velocity field at the bottom boundary. Our numerical model is simpler than reality since we do not increase the magnetic flux, but only simulate the observed photospheric flows. However, the applied shearing motions lead to injection of stress and free energy into the system, eventually leading to a substantial amount of magnetic reconnection.

The two horizontal components of the prescribed divergent velocity field can be written as

$$u_x(x, y) = u_1(x, y) \times u_2(x, y), \tag{5}$$

$$u_y(x, y) = \frac{2}{4.5} \times u_1(x, y) \times u_2(x, y). \tag{6}$$

The velocity field is presented in the top panel of Figure 4. The function $u_1(x, y)$ is the sum of two hyperbolic tangent functions of opposite signs. It reproduces the divergence of the motion of the magnetic polarities resulting from the emergence. The function $u_1(x, y)$ changes its sign at the averaged neutral line that separates the negative leading spots from the trailing positive pores located at the west of the parasitic polarity. This defines a line of positive flow divergence, which is simpler than the real diverging flows observed by *SOHO*/MDI.

The function $u_2(x, y)$ is a smoothed gate function which delimits the area over which the motions are applied, by mapping the observed elliptical shape of the flux emergence area. In order to avoid the formation of strong gradients by compressive

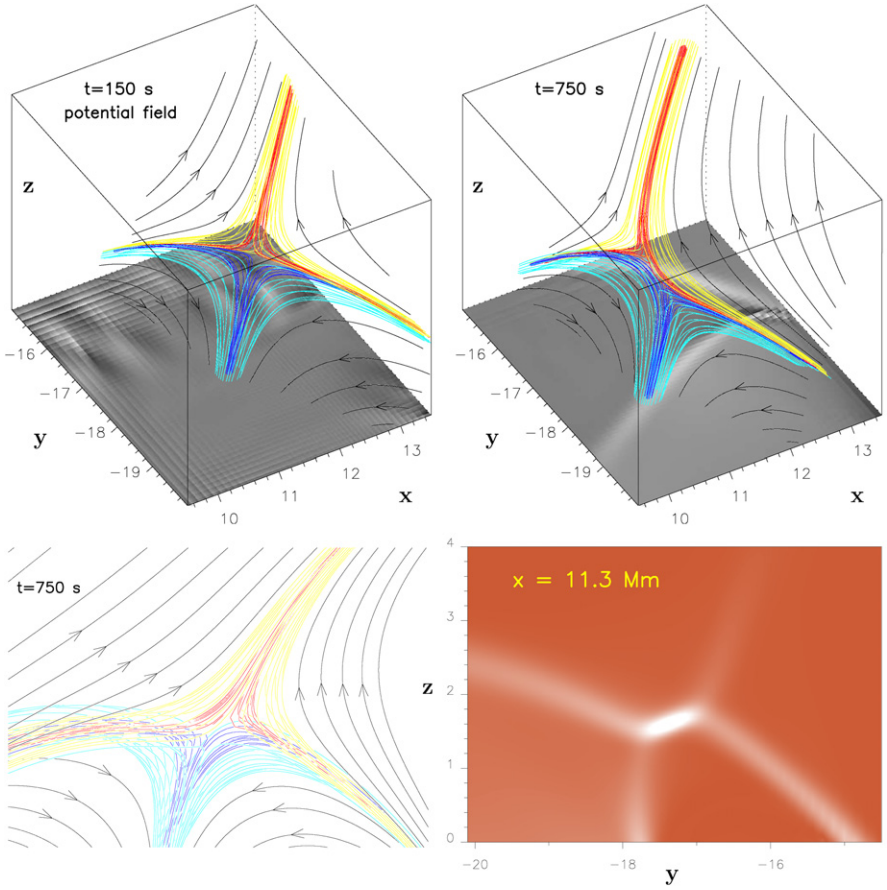

Figure 5. Deformation of the magnetic field around the null point during the simulation, at $t = 150$ s and $t = 750$ s. Spatial units are in Mm. The color field lines are integrated from small circles located around the spines at the photosphere ($z = 0$) and in the corona at $z = 4$ Mm (the top boundary of the plotted domain). The light and dark blue lines represent the inner spine and fan, whereas the yellow and red lines represent the outer spine and fan. Top panels: Bottom boundary ($z = 0$) distribution of the vertical electric current density $j_z(z = 0)$ in a grayscale coding. Black and white correspond respectively to values $j_{z,\min}(z = 0) = -13$ mA m^{-2} and $j_{z,\max}(z = 0) = 20$ mA m^{-2}. Bottom left panel: two-dimensional projection of the field lines on the plane (y, z) at the $x = 11.3$ Mm position of the null point and at $t = 750$ s. Bottom right panel: vertical two-dimensional (y, z) cut of the distribution of the current density $j(y, z)$ at $t = 750$ s and at $x = 11.3$ Mm (x abscissa of the null point, with the same FOV as the bottom left panel). The current density is represented with a redscale coding: red codes for no current density and white corresponds to $j_{\max} = 31$ mA m^{-2}.

and vortical effects at the boundaries of this region, $u_2(x, y)$ is defined by the product of two hyperbolic tangent functions having a weak slope. The factor 2/4.5 is used to reproduce the observed asymmetry of the respective magnitudes of the east–west and north–south motions of the magnetic polarities.

The velocity field (u_x, u_y) is gradually applied using a temporal ramp by multiplying the spatial velocity field with a time-dependent hyperbolic tangent function. This process allows an initial relaxation phase, between $t = 0$ s and $t = 150$ s, and leads to a phase with $u = \text{cst}$ for $t \geqslant 300$ s. The maximum amplitude for the driving velocity is equal to $u_D = 20$ km s^{-1}. Even though this value is larger than the typical observed photospheric velocities by a factor of 40, it sill remains subsonic and largely sub-Alfvénic as required for a coronal calculation (see Section 4.1), while it permits a reasonable computation time.

Overall, we note that the induced deformation of our longitudinal magnetogram (presented on the bottom right panel of Figure 4) agrees well with the description of the emerging flux in Section 2.2.

5. CURRENT SHEET FORMATION AND MAGNETIC RECONNECTION AT A SHEARED SPINE

At the end of the relaxation phase, at $t = 150$ s, the bulk of the initial residual forces, resulting from the fact that the initial configuration was slightly out of numerical equilibrium, have disappeared. Nevertheless some residual currents remain located at the boundaries. The large-scale homogeneous divergent velocity field introduced at the lower boundary induces a perturbation of the magnetic configuration in the active region, in which electric current sheets develop along various topological features.

The main region where intense current sheet develops is the vicinity of the coronal null point (see Figure 5). Even though a current sheet was expected to form here (compare Section 1), the following questions can only be answered with the numerical simulation: what is the local physical effect which drives its formation? Which mode of reconnection is favored with the present deformation of the outer spine; is it *fan reconnection* or *spine reconnection* or something more complex?

Figure 5 presents the evolution of the null-point topology. At each time the location of the null point is calculated automatically (see Section 3.1). Field lines which pass around the spines, and on both sides of the fan, have been integrated from initial points placed along two circles, being located around the photospheric footpoints of the inner spine and around a coronal section of the outer spine. These field lines do not trace the whole fan, because the amplitudes of the perpendicular eigenvectors of the asymmetric fan are different (see Section 3.1).

Between $t = 150$ s (time at which the forcing is initiated) and $t = 750$ s, a significant deformation of the null-point topological structures has occurred (top panels of Figure 5). The inner and the outer spine are no more aligned, as in the initial potential case, whereas the fan's curvature has not really changed. The topology closely resembles the cartoon model of a stressed three-dimensional null point presented in Antiochos (1996). In three-dimensional MHD simulations, this structure has first been reported in complex multi-null-point configurations (Galsgaard & Nordlund 1997) as well as in more recent line-tied single-null-point models (Pontin & Galsgaard 2007; Pariat et al. 2009). We also observe that the direction of the spines now presents an angle with the fan surface. Whereas the spines were initially perpendicular to the fan, at $t = 750$ s the spines present a small angle with the local normal to the fan in the vicinity of the null point. We checked that, as the current sheet developed, the angles formed between either of the fan eigenvectors with that of the spine gradually departed from their original $\pi/2$ values.

The shearing of the spine finds its origin in two large scale and two local effects in our simulation: first, the outer spine is rooted within the prescribed photospheric flow area, westward from the null point. Its slow photospheric deformations propagate eastward in the corona toward the null point. Around the null point, the associated Lorentz forces are converted into pressure forces, as the wave front passes through the $\beta \simeq 1$ shell. Second, the diverging flow pattern in the emerging flux area induces a footpoint separation of the field lines anchored in this region. This naturally leads to a slow expansion of these field lines in all directions. Since both the fan and the inner spine are rooted out of the photospheric flow area, and are not magnetically connected to it, the deformation of the magnetic field around the null point only occurs eastward of it.

The induced magnetic stress is locally driven by two MHD effects. First, the velocity component of the bulging field lines which is perpendicular to the fan induces a slow compression of the three-dimensional null point. This leads to a flattening of its X-shape in two dimensional, as in the classical three-dimensional X-point collapse picture (e.g., Parnell et al. 1997; Mellor et al. 2003). But this compression is strongly slowed down in our simulation, due to strong pressure gradients that develop inside the $\beta \leqslant 1$ shell. Second, the shearing of the outer spine, combined with the fan-aligned velocity component of the expanding field lines, leads to shearing motions of field lines on the western side of the fan around the null point. This process is not affected by pressure gradients, since the field line motions occur perpendicularly to it. This differential shearing on the outer side of the fan leads the whole western part of the null-point magnetic configuration to slide sideward relatively to its other (inner) half (as in the picture of Antiochos 1996). This behavior combined with the viscous effects results in a vorticity sheet of finite width along it. Such a vorticity sheet located within a null-point fan naturally produces a co-spatial current sheet, as well as new converging motions toward the null point on both sides of the fan, both being required to drive null-point reconnection (see the Appendix). All these effects eventually result in a modification of the topological structure, and in the formation of a current sheet in an extended weak magnetic field area that has a nearly fan-aligned double-Y shape in two-dimensional slabs (as plotted in Figure 5), and eventually in magnetic reconnection.

The fan-aligned currents being the more intense agrees with the fact that the forcing was induced mostly by a shearing of the outer spine. Pontin et al. (2007a) had shown that intense currents in the fan were induced by the perturbation of the spine, and were even more likely to develop when taking into account the effect of compressibility (Pontin et al. 2007b). The development of intense current at the null itself is also in agreement with the type of forcing that we imposed. Pontin et al. (2007a) showed that the twisting of the spine is less efficient to form currents at the null itself compared to shearing perturbations. The formation of current sheets allows the efficient development of the reconnection mechanism. The effect of the reconnection is to attempt to bring the two spines back into alignment (Antiochos et al. 2002). This is exactly what happens in our simulation. More precisely, the fact that the more intense currents are fan-aligned also implies that both *fan reconnection* and *spine reconnection* (in which the field lines flip from one spine to the other) can occur, depending on which field lines are traced and followed (Pontin et al. 2005). However, one should note that only *spine reconnection* can lead to a real transfer of magnetic flux between the two connectivity domains, i.e., from one side of the fan to the other, as occurs in our simulation.

Looking at the distribution of the vertical component of the current j_z at the bottom boundary, (see Figure 5, top panels), one can see that two arcs of currents have formed at $t = 750$ s: one corresponds to the fan surface (the one in the back, for $j_z \leqslant 0$) which corresponds to the ribbon RC, and another one (of $j_z \geqslant 0$) in the middle of which the inner spine is anchored (in the center of the top right panel of Figure 5). This second current sheet is spatially located at the same place than the ribbon RA. At this stage, one can wonder whether this long current sheet relates to that of the null point in the corona. In fact, several two-dimensional slabs in (y, z) at various x values around the null point show that this photospheric trace of current cannot be the prolongation of the current sheet of the null point. Since this photospheric sheet elongates as a function of time, and since the maximum of the intensity gradually shifts eastward (decreasing x), it may rather be related to the spine-aligned current sheet (anchored at $y = -18$ Mm as seen on the bottom right panel of Figure 5). Indeed, as reconnection proceeds, the separatrix of the null point jumps from field line to field line (Antiochos et al. 2002), which in our simulation leads to a slow drift of the inner spine in the east direction. In this picture, the photospheric current sheet would then be formed only by residual currents that have been accumulated while the spine was moving along the photosphere, and that could dissipate in a longer timescale than that of the displacement of the spine. To test this hypothesis it is necessary to look at the evolution of the null point and the spine while reconnection takes place, which we discuss next.

6. RECONNECTING AND SLIPPING FIELD LINES

6.1. Evolution of Connectivities

By plotting field lines from a fixed footpoint and by observing the evolution of their conjugate footpoint, one can follow the evolution of the magnetic field connectivity during the simulation.

The field lines displayed in Figure 6 are plotted from a fixed footpoint located in the positive polarity surrounding the large parasitic polarity. These field lines are rooted outside of the region where the motions are prescribed. Thus, at each time, each field line is integrated from the same footpoint position at $z = 0$. The observed field line evolution is thus only due to the evolution of the connectivity induced by the evolution of the system. Initially, the plotted field lines (red,

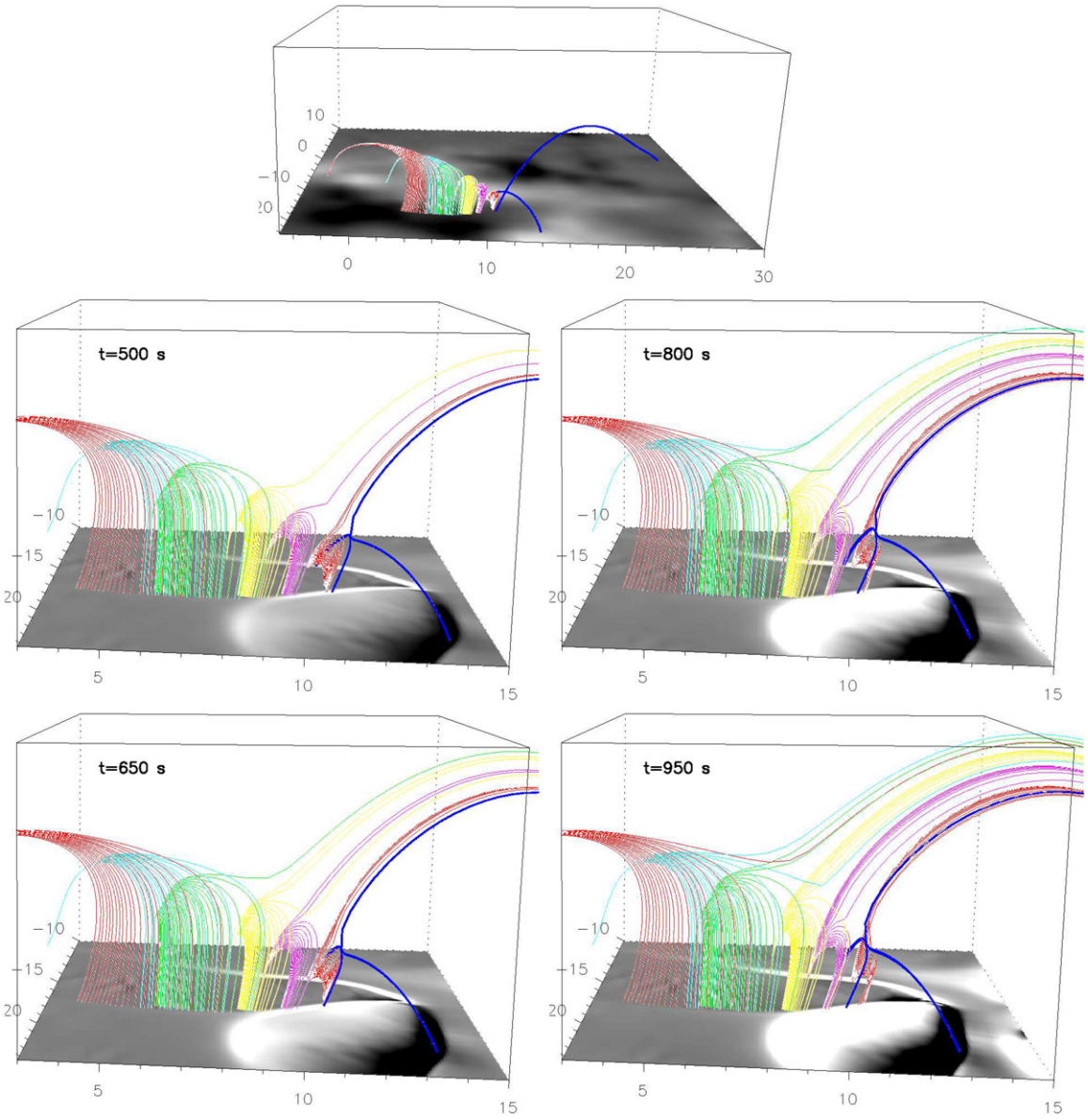

Figure 6. Evolution of selected field lines. The dark-blue field lines are spine and fan field lines passing through the null point. The other colored field lines are plotted with fixed footpoints in a positive flux area, located at the north–east of the null point and out of the prescribed boundary flows. Top panel: initial ($t = 0$ s) configuration: all colored field lines are initially located below the fan surface of the null, in the inner connectivity domain. The distribution of the photospheric vertical magnetic field $b_z(z = 0)$ is coded in scale of gray. Lower panels: evolution of magnetic field lines in the inner connectivity domain. The distribution of the vertical electric current density $j_z(z = 0)$ at the bottom boundary is gray shaded. This grayscale coding is the same for all panels. Black and white correspond respectively to the values of $j_{z,\min}(z = 0) = -50$ mA m^{-2} and $j_{z,\max}(z = 0) = 50$ mA m^{-2}.

(An mpeg animation of this figure is available in the online journal.)

pink, yellow, green, light-blue, and red again) are located below the fan surface, in the inner connectivity domain, connecting the positive polarity and the parasitic polarity. For each group, field lines are regularly plotted along a small segment, each segment being approximatively located at the same distance from the fan. The dark-blue field lines correspond to some separatrix field lines passing through the null point. They are integrated at an infinitesimal distance $\leqslant$ 0.01 Mm from the null point which location is computed at each time by an iterative calculus. The dark-blue field lines trace the position of the spines and of two lines that belong to the fan surface and which emanate from the null along the dominating eigenvector. These particular lines trace the evolution of the separatrices throughout the evolution of the system.

The four lower panels of Figure 6 (see also the movie available in the electronic version) present the temporal evolution of these field lines, in the region located around the inner spine. It clearly appears that at $t = 500$ s some field lines have reconnected at the null point: some red, pink, and yellow lines are now connected to the leading sunspot and now belong to the outer connectivity domain. Detailed analyses with small timesteps show that all the field lines reconnect at the null point itself when they change their connectivity from below to above the fan surface. The nonfixed footpoints of the field lines flip from the vicinity of the inner spine to the vicinity of the outer spine, as in the *spine reconnection* regime.

As the simulation evolves, more and more field lines reconnect at the null point. This induces a displacement of the null

point eastward, with a corresponding motion of the separatrices (see the evolution of the dark-blue lines in Figure 6). The footpoint of the inner spine moves eastward and eventually passes the location of the footpoints of the red field lines rooted in the parasitic polarity. This motion cannot be attributed to numerical errors of the trilinear interpolation code since the null point has been moved by several mesh points. However, the displacement of the null and the separatrices is rather small, being only of the order of 1–2 Mm.

We also note that field lines do not reconnect randomly: the sequential order of reconnection along the fan has a counterclockwise (eastward) direction. In Figure 6, one sees that the red field lines (those closest to the null) are the first to reconnect and that a large number of them do. Then the pink field lines start to reconnect, but the number of field lines that have reconnected is smaller. Later on the yellow field lines start to reconnect, while a larger number of pink field lines have now reconnected. The green field lines are next to reconnect, while the number of reconnected yellow line has increased. Eventually fewer red field lines (those closest to the null) reconnect while the other groups of field lines keep reconnecting. Overall this shows that most of the reconnection initially takes place for field lines closer to the null point, and that it eventually progresses further toward the east.

By plotting several groups of field lines with fixed footpoints rooted along the southern part of the parasitic polarity, within the inner connectivity domain (using the same methodology as with the field lines plotted in Figure 6) and by tracking their evolution in time, we noted that the first field line to reconnect at the null point are the one rooted the further east to the null point. We then observe that reconnection sequentially involve field lines located westward. Thus, the reconnection of the field lines has also a counterclockwise propagation along the southern part of the fan. This evolution of the reconnection is due to the asymmetric geometry of the current sheet at the null point which is induced by the asymmetric magnetic configuration (see Section 5).

Some caution has to be taken when interpreting the sequence of reconnection in three dimensional: classically, out of two field lines, the first one to reconnect is the one rooted the closest to the fan surface. In our model, each group of colored field lines presented in Figure 6 is plotted along a small segment locally oriented orthogonally to the fan, all of them having comparable lengths and being placed at roughly equal distances from the fan. In addition, in each group, consecutive field lines are located at the same fixed distance from each other along each segment. This means that within each group the rate of field-line reconnection is an indicator of the local reconnection rate, and that the observation of the first field lines to reconnect in each group still gives an idea of the sequence of reconnection. The rate of field-line reconnection increasing from west to east shows that the local reconnection rate progresses with a similar pattern.

As field lines reconnect counterclockwise, particles are accelerated along these field lines and emissions are expected to originate from further and further eastern regions away from the null point (in the north section of the ribbon), leading to a counterclockwise spreading of the brightening along the fan ribbon. This agrees well with the *TRACE* observation (compare Section 2.1) that the quasi-circular ribbon RC extended counterclockwise (initially eastward) during the flare.

Another particularly interesting feature noted in the simulation is that prior to reconnecting at the null point, several field lines slip westward toward the inner spine of the null (see Figure 6 and the corresponding movie available in the electronic version). All the field lines slip following the same path, along the arc of intense vertical electric current density j_z (plotted in grayscale coding in the four bottom panels of Figure 6) which was previously discussed in Section 5 and there associated with the inner spine. We note here that the location and the length on which this slipping motions occur correspond to the location and the extent of the ribbon RA (compare Section 2.1). Estimating the slippage velocities of these field lines, we obtained a mean value of 30 km s^{-1} as long as the field lines are further away than 1 Mm from the spine, which is largely sub-Alfvénic. At a relatively small distance (1 Mm) from the null point, the slippage velocities increase significantly and become super-Alfvénic. We observe that the closer the field-line footpoints are from the footpoint of the spine, the larger is the velocity: the field lines accelerate as they approach the magnetic null point.

This slipping motion toward the null point provides an additional proof in favor of the counterclockwise propagation of the emissions along RC. Indeed, the further east the fixed footpoints are in the positive polarity close to the fan, the further their nonfixed footpoints are far from inner spine (compare Figure 6). Thus, the larger the distance the field line will have to cover slipping toward the null before reconnecting and the longer it will take to reach the null starting with a slower slipping velocity. This means that the field lines located closer to the null are likely to reconnect before those located further east along the fan surface. Also, the fact that initially a larger (resp. smaller) number of field lines are located on the western (resp. eastern) part of the ribbon RC, close to (resp. away from) the null point, indicates that a larger (resp. smaller) portion of the magnetic field flux around the inner spine is rooted near the west (resp. east) part of the ribbon RC. So, when reconnection starts, for a given reconnection rate at the null point, most of the reconnected flux will therefore first involve the western part of the ribbon RC, i.e., field lines which do not need to slip a lot to reach the null, and which slip with higher velocities since they are closer to the null. Later, field lines located further east will start to reconnect, after having slipped over larger distances. This explains why the reconnection seems to move eastward, and why the maximum emission along the ribbon RC follows a counterclockwise emission.

A similar slipping behavior is also observed in the region where the outer spine is located. Figure 7 (and the corresponding movie available with the electronic version) displays the footpoint of the very same field lines plotted in Figure 6, after they have reconnected at the null point. The temporal evolution of these field lines shows a westward slippage of the field line footpoints, away from the outer spine. Still, the slippage is less pronounced than in Figure 6, before the null-point reconnection. This is partly due to the fact that these field lines are now rooted to a region where the boundaries flow are prescribed (as can be seen in Figure 7). The overall motion is thus the superposition of the westward slipping motion and the opposite eastward photospheric flow. The westward slipping motion can nonetheless be analyzed by following some particular field lines in the reference frame of the moving flux concentrations at $z = 0$. In Figure 7, two field lines have been selected (a yellow line in the left column and a red one in the right column) and marked with an arrow. These post-reconnection field lines clearly present a westward slipping motion in the outer connectivity domain, going away from the outer spine (plotted in dark blue). As for the slippage of the field lines in the inner connectivity domain, their slippage velocity decreases as the

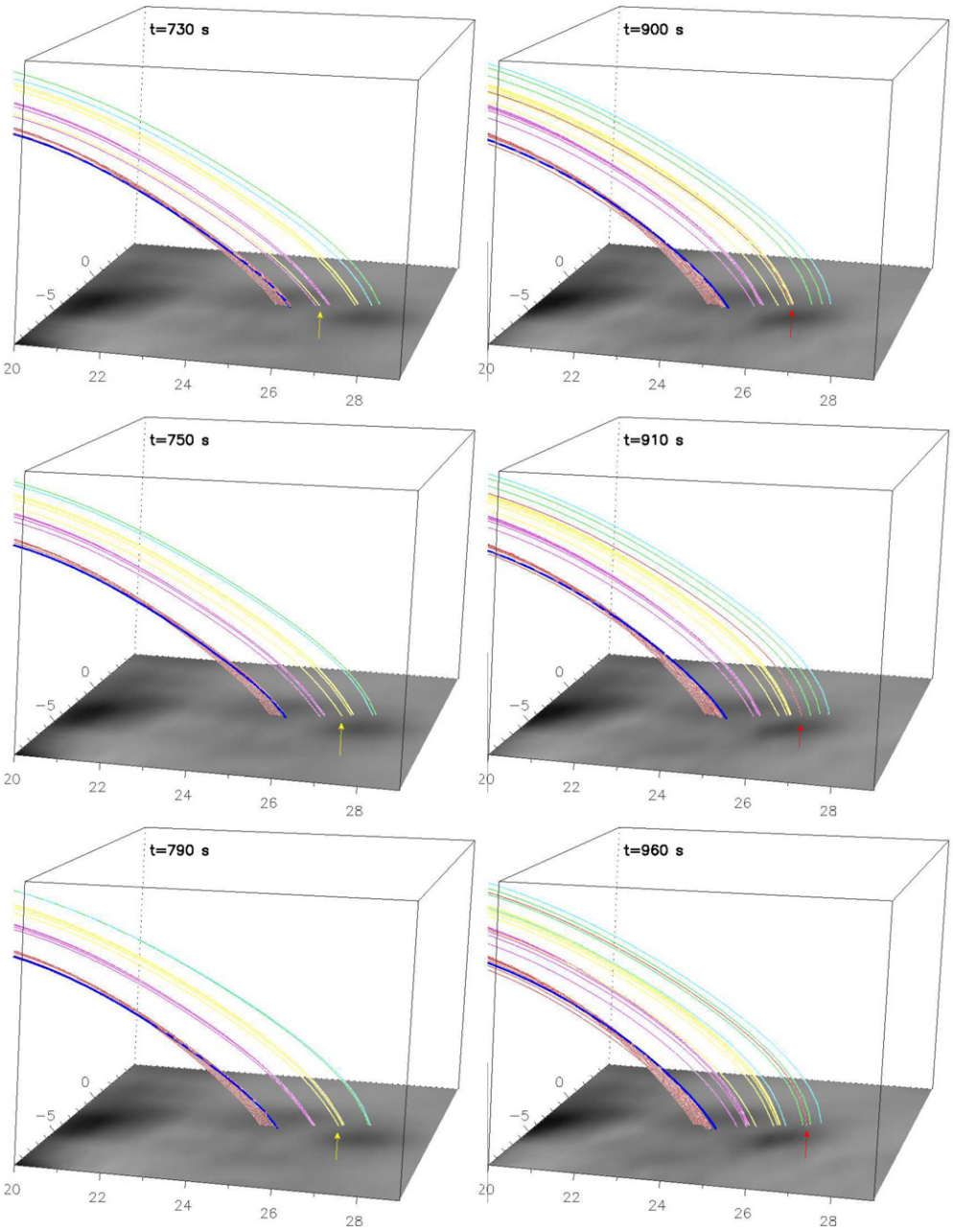

Figure 7. Evolution of some reconnecting field lines around the outer spine. The grayscale coding for the distribution of the magnetic field $b_z(z = 0)$ is the same as the top panel of Figure 6. The evolution of the footpoint positions of two particular slipping field lines are marked by colored arrows (yellow in the left column, red in the right column). Spatial units are in Mm.

(An mpeg animation of this figure is available in the online journal.)

field line footpoint moves further from the footpoint of the outer spine.

This westward motion in the outer spine probably provides an explanation for the evolution of the emission pattern during the fading of RB. In the later phases of the flare, as the dissipation of the current sheets is almost over, fewer field lines will reconnect at the null and then slip westward. The overall effect would be that the emission would be reduced first in the east end of the ribbon, while some emission would still originate from the western part of the ribbon, where previously reconnected field lines would still be slipping. As the last reconnected field lines would end their slipping motion, the brightening would progressively decrease toward the west, as observed in RB (compare Section 2.1).

The evolution of field lines rooted inside the parasitic polarity, close to the inner spine, and the motions of the field lines which have reconnected, close to the outer spine, are very likely to explain the dynamic of the spine ribbons RA and RB. This statement assumes that the slipping field lines, embedded within intense current layers, carry enough energy to generate an emission at their footpoints. At this stage of the analysis, one can wonder about which mechanism can explain the observed slippage of the field lines before and after they reconnect and the energy deposited within them? The classical interpretation for ribbons elongation involves the motion of the reconnection site, as described in Section 3.2, but this model does not fully allow us to understand the formation of the ribbons in this particular case. Indeed, in the present simulation, the extension of the

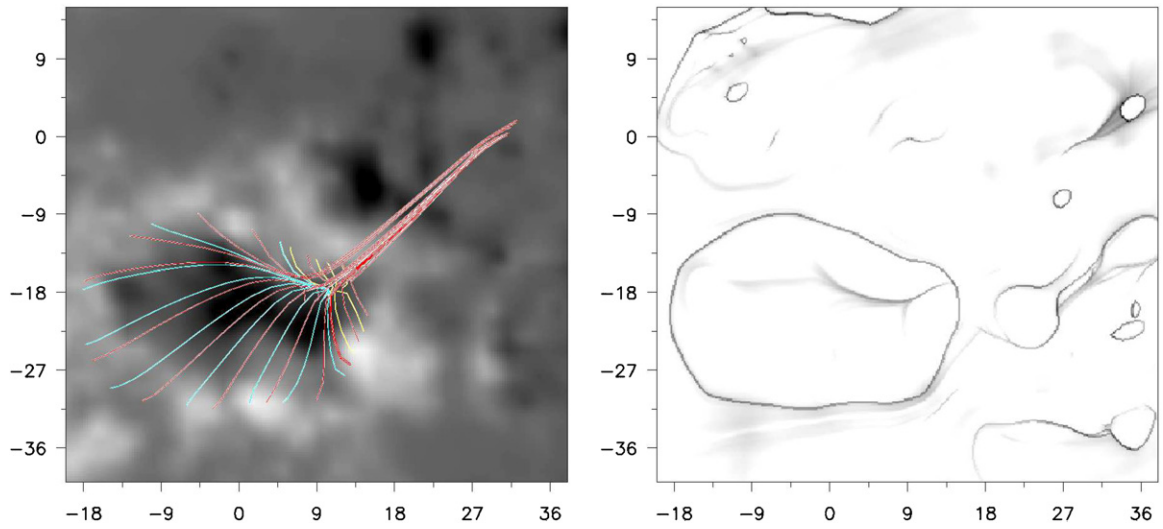

Figure 8. Initial ($t = 0$ s) distribution of the vertical magnetic field $b_z(z = 0)$ (left panel) and of the squashing factor Q (right panel) at the photospheric level ($z = 0$) plotted with an inverse-grayscale coding: the lowest values of Q (in white) are inferior to 20, while the darker regions correspond to Q values up to 10^9. In the left panel, the field lines are the same as those plotted in Figure 3. The spatial units are in Mm and the coordinate system is the same as in the previous figures.

intense-current sheet is limited to the region separating the two sheared spines (compare Section 5). Therefore, no important displacement of the reconnection site is allowed within the current sheet. In addition, the displacement of the null point, i.e., the intense-current sheet and therefore of the reconnection site, is much smaller than the elongation of the ribbons, as well as smaller than the distance over which the field lines slip. The null point and the separatrices associated present only a motion of the order of 1–2 Mm while the ribbons are an order of magnitude longer (∼20 Mm). The evolution of the null point is also several times smaller than the displacement of the magnetic polarity in the photospheric region where the forcing is imposed. The imposed boundary motion is thus very unlikely to explain the observed elongation of the ribbons. Also our prescribed photospheric forcing is already slightly broader than what is observed (compare Section 4.2) so, completely unrealistic boundary motions would have to be prescribed to obtain a displacement of the null that would approach the size of the ribbons.

Therefore, in the present case, we do not believe that the evolution of the null is responsible for the formation and elongation of the spine ribbons. Another mechanism must be involved, as discussed hereafter.

6.2. Separatrices Embedded in QSLs

When reconnection occurs without true three-dimensional separatrices, Priest & Forbes (1992) suggested that magnetic field lines must slip along each other, within so-called magnetic flipping layers. Priest & Démoulin (1995) and Démoulin et al. (1996) then introduced the concept of three-dimensional QSLs. QSLs are narrow volumes across which the magnetic field connectivity remains continuous, but where it has very strong variations. A QSL is a purely three-dimensional object, in which the connectivity gradients are the largest in the sub-region where the squashing degree Q (defined by Titov et al. 2002) peaks to its maximum value; domain known as the hyperbolic flux tube (HFT). Priest & Démoulin (1995) proposed that magnetic flipping occurs in a QSL: field lines simply exchange their connectivity with that of their neighbors, as one of their footpoints is displaced in time across a QSL. Continuous reconnection between neighboring field lines leads to a continuous exchange of connectivity and to the apparent slippage of a field line plotted from a fixed footpoint. Field lines slippage was then reported in MHD simulations of magnetic reconnection in a straight and stressed HFT (Pontin et al. 2005). In a more general QSL and HFT geometries. Aulanier et al. (2005b) demonstrated numerically that, similarly to classical separatrices, thin current sheets are likely to form within QSLs, where the squashing degree Q is the highest. Then, Aulanier et al. (2006), observing the same slipping behavior, proved that when QSLs are thin enough, the slippage velocities of the field lines can be so fast that Alfvén waves traveling along them do not have the time to propagate from one footpoint to another. This is the so-called *slip-running reconnection*. It follows that on MHD timescales, such slipping field lines can physically behave nearly as if they were reconnecting at separatrices, i.e., as if they instantaneously changed their connectivities. These recent theoretical results support the numerous association of observed flare ribbons with QSL (see e.g., Démoulin et al. 1997; Mandrini et al. 1997). More recently, some slippage of post-reconnected coronal loops have been identified in X-ray observations by *Hinode* (Aulanier et al. 2007). The topological study of these slipping loops showed that the loops were very likely to be located close to a QSL.

QSLs are thus very good candidates to explain the evolution of the connectivity and the slippage of the field lines in our present simulation. However the coexistence of QSLs and of a null point is a priori not straight forward. To confirm this hypothesis we computed the squashing degree Q along the bottom boundary. The method used to compute Q is identical to the one used in Aulanier et al. (2005a, see extended description therein; Section 2.3). The computation is done iteratively on a grid of 201 × 201 points placed at $x \in [-20, 38]$ Mm, $y \in [-40, 15]$ Mm in the magnetogram. The grid is refined 2 times keeping only the points where the values of Q are the highest. With this method, the real maximum values obtained for Q are unlikely to be exact. The present magnetogram contains real separatrices where the Q is theoretically infinitely large. Therefore we do not attempt to compute precisely the value of the squashing degree Q at each point, which would involve unnecessary computation time. Here we mostly want to focus on the localization of the broad QSLs. The present computation allows us to localize the QSL where Q is larger than 20 without really focusing on the precise widths and maximum values of Q.

The result of the computation is displayed in the right panel of Figure 8. On the left, several closed drop-shaped structures are present. These structures correspond to the trace of bald patch separatrices present in the emerging region. These structures will be thoroughly studied in a forthcoming paper.

The main feature that can be observed is the large circle/ellipsoid of high Q. This circle is located slightly at the exterior of the inversion line of the magnetic field. The field lines plotted in the left panel of Figure 8, which had been already plotted in Figure 3, highlight the spine-fan topology. The footpoints of the fan section of the field lines are exactly located along this high-Q circle: it thus maps the intersection of the fan surface with the photosphere.

Similarly, within the fan circle and in the upper right corner, two other structures of high Q can be found and related to the inner and the outer spine, respectively. Although, while the location of the footpoints of the spine field lines is relatively compact, one observes that the region of high Q is more elongated and has a much larger size than the surface of the field lines tracing the spine. Whereas the spines should be associated with almost point-like separatrices in the photosphere, Figure 8 shows that the regions of very high Q ($Q > 10^8$) at the spine footpoints are surrounded by broad and extended regions of intermediate values of Q (i.e., QSLs) not only around the spine, but also around the fan. This indicates that the fan and spine separatrices are embedded in more extended QSLs. Note that the fan-related QSL could actually have been directly figured out from the connectivity of the field lines plotted in Figure 6. Within each group of field lines, while the distance between the footpoint of two consecutive plotted field lines is extremely small, the distance between their two respective opposite footpoints is much larger. This is a strong evidence that the connectivity gradients are large and therefore that these field lines are located within a QSL.

Around the inner spine, the QSL is extremely elongated. The length of this QSL is of the order of 12 Mm and reaches even 22 Mm if one includes the region of very low Q on its left (see Figure 8). It is also particularly striking that the shape and location of this QSL matches extremely well the location of the ribbon RA (compare Figure 1). Similarly the outer spine is also surrounded by a wide QSL which extends over $\sim$10 Mm and whose shape can relate to the ribbon RB. The analysis of the map of the squashing degree Q at $z = 0$ shows that, even though the location of the spine coincides with the location of the ribbons, the latter are far more precisely related to the QSLs (as in Démoulin et al. 1997; Mandrini et al. 1997).

Analyzing the plasma velocity in the simulation, we observed that it is completely uncorrelated with the slippage velocities of the field lines. The plasma velocity is actually a combination of the compression of the field lines along the x-axis, induced by the bulge of the field lines rooted where boundaries flow have been prescribed, and a two-dimensional flow pattern generated by the reconnection process in the HFT, which can be assimilated to a reconnection in a two-dimensional X-point within (y, z) slabs. But the field lines slip westward, opposite to the plasma flow. The motion of the field lines at the vicinity of the inner spine are therefore not bulk motions, and are basically due to the continuous changes of connectivity resulting from a slipping and a slip-running reconnection (Aulanier et al. 2006).

Figure 6 shows that the nonfixed footpoint of the field lines are initially located along the inner QSL. In the first part of the evolution of the system, the field lines slip along the QSL from east to west faster and faster toward the null point and the inner spine. Some field lines eventually reconnect at the null point and there Figure 7 shows that the nonfixed footpoint is now located within the QSL surrounding the outer spine. As the system evolves, the field lines slip away from the outer spine, slower and slower, but still within the QSL. As discussed above, the slippage of the field line is a typical characteristic of reconnection at a QSL and the slippage velocities are the largest when the field lines slip into regions of high Q (Aulanier et al. 2006, 2007). In the present simulation, the slippage of the field line is therefore the direct consequence of the existence of the QSLs surrounding the spine separatrices.

7. CONCLUSION: ON THE ORIGIN OF DRIFTING OF UV EMISSION ALONG RIBBONS IN A NULL-POINT TOPOLOGY

In the present paper, we have thoroughly studied the formation and development of a quasi-circular ribbon and of two elongated sheet-like ribbons during a C-class flare which occurred on 2002 November 16 within AR 10191. Using UV observations from *TRACE*, *SOHO*/MDI magnetogram, a potential extrapolation of the magnetic field, and a three-dimensional MHD numerical simulation of this event, we argue that

1. The active region included a coronal null point. The fan surface originating from the null point divided the active region into two distinct connectivity domains, each of them including a spine separatrix field line.
2. The C-class flare followed an emerging flux event in the center of the active region. As in the model of Heyvaerts et al. (1977), the emergence of the magnetic field induces the injection of magnetic free energy and eventually destabilizes the magnetic configuration leading to a release of the free magnetic energy via magnetic reconnection. Using a MHD numerical simulation (similar to the one described in Aulanier et al. 2005a), and emulating the observed emergence by a divergent boundary shearing motion in the interspot region, we demonstrated that this emergence should indeed lead to the formation of intense current sheets.
3. The narrowest currents in the MHD simulation form in the vicinity of the null point and are due to a shearing of the spines relatively to the fan surface. The driving motions at the bottom boundary induced a perturbation which led to a sensitive modification of the null-point geometry. The spines departed from orthogonality to the fan surface and both developed an angle relatively to the local vertical. The spines lost their co-alignment after having been torn apart.
4. The quasi-circular ribbon was linked with the presence of the fan separatrix surface originating from the magnetic null point. Its shape corresponded to the quasi-circular mapping of the fan surface at the photospheric level. This is in strong agreement with the classical model of confined flares (e.g., Priest & Forbes 2002) in which the ribbon emissions are due to the particles accelerated at the reconnection site, flowing along the separatrices field lines and eventually interacting with the denser layer of solar atmosphere.
5. However, the two other observed ribbons could not be explained by particles solely flowing along spine field lines. Even though these ribbons could be spatially associated with the inner and outer spines, the elongation of spine singular field lines is too small to account for the elongation of ribbons. Thus, they could not be directly interpreted as the consequence of particles flowing along statics spine

field lines. In addition, the numerical simulation showed that, even using important shearing driving motions, the null point and the spines only moved over a very small distance relatively to the size of the ribbons during the evolution of the system. Therefore, the ribbons could not be explained by the dynamic motions of the spine field lines nor by the dissipation of residual currents.

6. These spine ribbons were actually due to the presence of QSLs (Démoulin et al. 1996) surrounding the spine field lines. Computing the squashing degree Q (Titov et al. 2002), we found that extended photospheric QSLs were present and matched very well the location and shape of the observed extended spine ribbons as well as that of calculated photospheric current sheets. We determined for the first time that separatrices can be embedded in larger QSLs. The present study therefore confirms that significantly intense currents naturally build-up within the QLSs (Aulanier et al. 2005b) and that electric currents match well the location of ribbons.
7. Slipping/slip-running reconnection (Aulanier et al. 2006) and null-point reconnection can occur sequentially. The evolution of the field lines showed that field lines first encountered slipping followed by slip-running reconnection (starting roughly at a distance of 1 Mm from the inner spine) while they slipped in the QSLs surrounding the null-point separatrices. Estimation of the apparent slippage velocity indicates that, in the present simulation, the slipping reconnection regime is dominant. The apparent displacement of field line footpoints mapped the photospheric QSL and the ribbon associated with the first spine. The field lines eventually reached the separatrix surface and reconnected in the more traditional "cut-and-paste" way. A second phase of slip running followed by slipping reconnection then occurred as the field lines slipped away from the separatrix surface. Doing so, the apparent motion of the footpoints mapped the photospheric footprint of the QSL and the ribbon of the second spine. Spine ribbons are thus very likely to be induced by particles accelerated by the parallel electric field of the electric currents formed within the QSLs, and propagating along field lines which are slip reconnecting.

From our simulation, we thus show that slipping reconnection and traditional "cut-and-paste" reconnection can both occur sequentially in a given magnetic configuration. The parameter which controls which mode of reconnection occurs is the squashing degree Q. With intermediate values of Q, field lines slip at moderate velocities. The slipping is only an apparent motion since it is the connectivity of the field lines which is continuously changing within the QSL, between neighboring field lines. Field lines lying within a volume where Q exceeds a critical value $Q_{\rm slpr}$ (very close to the spine), have their apparent slipping velocities which can become larger than the Alfvén speed. This mode of reconnection has been defined as "Slip-running reconnection" in (Aulanier et al. 2006). On the MHD timescales, the field lines would then behave as if they were reconnecting at a separatrix. Finally, when Q is infinitely high, which qualifies a separatrix, "cut-and-past" reconnection occurs with an instantaneous jump of connectivity.

Several of the field lines presented in Figures 6 and 7, experience these three modes of reconnection. As the system evolves, the field lines eventually become located in the region of moderate Q in which mild currents are present. They start to reconnect within the QSL, and when plotted from fixed footpoints, they slip toward the null point. As they continuously reconnect with neighboring field lines, they slip within volumes of higher and higher Q. As these lines reach regions of larger current densities, the reconnection rate increases and their apparent slipping velocity too. Eventually the field line apparent velocity becomes equal to the Alfvèn speed: the value of Q is equal to $Q_{\rm slpr}$. Then, within the volume where $Q > Q_{\rm slpr}$, the field lines slip run toward the separatrix. A *spine reconnection* occurs next: there is a transfer of flux from the inner connectivity domain to the outer domain as a given field line crosses the fan surface. The field lines, now located in the outer domain, are still lying within the QSL surrounding the null-point separatrices, in a region of very high Q. They slip run away from the fan surface, reaching regions of lower and lower Q. Their slipping velocity decreases and they eventually enter domains where the connectivity gradients are extremely low and where no currents are present.

Observational evidences (e.g., Fletcher & Hudson 2001) and standard models (Priest & Forbes 2002) indicate that UV ribbons and HXR emissions during flare are the consequence of same mechanism of accelerated particles flowing down along reconnected magnetic field lines. Therefore, the different modes of reconnection presented in the present paper can not only explain some of the observed properties of the formation of ribbons, and especially their elongation, but also displacements of HXR sources during flares (e.g., Bogachev et al. 2005). Slipping reconnection, in region of low Q would lead to slow HXR footpoint motions while slip-running reconnection, in region of high Q would lead to fast HXR footpoint motions. Finally null-point reconnection would induce a jump of the HXR footpoint position (as frequently observed, e.g., Krucker et al. 2003, 2005).

We have not addressed the nature of the precursor of the flare (Section 2.1), but the shape of the related brightenings are suggestive of low-energetic pre-flare null-point reconnection: the north–west part of RC would correspond to fan emission, and the perturbed loop is suggestive of the spine field line. There is no evidence of the bright kernel which would trace the footpoints of the outer spine. Outer spine emissions are also absent in the early phase of the flare, before the north part of RC saturates: RB only appears 30 s after RA/RC. In both cases, this feature is not readily explained by our simulation. However, the association of QSL and three-dimensional null-point topologies may be able to account for these observations: QSL slipping reconnection may occur and may release magnetic energy before field lines reconnect at the null point. In this picture, the QSL may be responsible of the precursor and the early brightenings along RA/RC, without requiring any outer spine counterpart. In the absence of such an early slipping reconnection, why would the outer spine footpoints brighten only a relatively long time after the whole circular fan ribbon? Some mechanism should then be invoked to explain the delay to obtain an emission between the different photospheric footpoints of the field lines involved in the null-point reconnection. However, our model does not address this issue.

In addition, the slipping directions of the field lines in the simulation can account for several of the observed properties of the ribbons. The westward motion of the field lines around the outer spine can explain the reduction of the emission of the ribbon RB in that direction. The simulation also provides some clues concerning the spreading of the emission in the counterclockwise direction along the quasi-circular ribbon RC. The presence of QSLs implies a sequential order of reconnection

for the field lines and thus a specific direction of elongation for the brightenings along RC.

However, our simulation is not able to explain all the dynamics of the flare. The elongation of RB in both east and west directions during the impulsive phase of the flare cannot be explained by the simulated slipping pattern of the field lines close to the outer spine. One possible reason for this discrepancy may originates from the limitation of our magnetic field extrapolation (Section 3.2) not being able to match the exact position of the outer spine. It may be located in the center of the QSL. Therefore, the reconnected field lines, in the outer domain, would have diverging slipping motions away from the outer spine in both directions which would account for the observed spreading of RB. Our model cannot confirm or falsify this conjecture.

Our simulation provides a general framework to understand the formation of the UV ribbons and HXR emissions but cannot completely address the precise details of this type of phenomenon. Already with three-dimensional separatrix reconnection, since no unique flux-conserving velocity exists (Priest et al. 2003), there is no one-to-one reconnection correspondence of reconnecting field lines (Hornig & Priest 2003). It implies that in three dimensions, the description of a reconnection sequence for field lines depends on the particular selection of their starting points. With QSLs, the picture is even more complex: Aulanier et al. (2006) showed that, as QSL reconnection proceeds, a large sets of field lines are reconnecting with one another, and, depending on their starting footpoints, can slip in one or the other direction. The current sheets having a given three-dimensional structure, an extremely large number of field lines can reconnect simultaneously. Tracing them from different starting point may lead to significantly different behaviors. The overall consequence is that the observed structure of a ribbon, its formation and its evolution is very sensitive to the specific details of the acceleration of the particles at the reconnection site. Thus, the precise distribution of the flux of accelerated particles among the reconnected field lines is of primary importance to explain the ribbon evolution. The key question is: "At the reconnection site, in which reconnecting field lines are the particles accelerated?" The precise description of the reconnection in a complex three-dimensional current sheet goes beyond the possibility of the MHD approximation and cannot be directly approached by our model.

Nonetheless, topological studies can bring some answers about the global properties of the formation of ribbons. The quasi-circular-shaped ribbon studied in the present paper is only a new item in the long list of works which demonstrated that the location of the ribbon is governed by the topological structure (e.g., Mandrini et al. 1991; van Driel-Gesztelyi et al. 1994; Démoulin et al. 1997). The present topological study can also allow us to understand the two-stage evolution frequently observed with arcade flare ribbons: a fast parallel spreading/expansion of the ribbon along the polarity inversion line followed by a slower perpendicular expansion (Moore et al. 2001; Qiu 2009). In the frame of QSL reconnection, the first phase can be understood as the consequence of the slippage of the magnetic field lines along the QSL (in which the separatrix is embedded), while the second phase would more classically be due to the apparent motion of the topological structure itself (QSL domain and null point/separatrices). The apparent velocity of the slippage, being much larger than the velocity of the topological structure, naturally accounts for these two distinct phases. This would imply that separatrices are frequently observed to be embedded in QSL in the solar corona. This result remains to be demonstrated for a larger sample of active regions.

Finally, we highlighted that the shearing of the spine lead to intense electric currents. This tearing of the spine had been predicted by Antiochos (1996) as an efficient way to form current at the null point, and recently been observed in numerical simulations (Pontin et al. 2007a; Pariat et al. 2009). The most intense currents develop along the fan surface, between the two points where the spines intersect with the fan. The present study confirms that stressing the spine is an efficient way to form intense current sheet in null-point reconnection. Pariat et al. (2009) claimed that the shearing of the spine was accompanied by the formation of a "null line" joining the anchorages of the two spines on the fan surface, but Pontin et al. (2007a) argued against the formation of such a null line. The present simulation does not have a resolution large enough to fully address that question. Further investigation will be necessary to understand the formation of a current sheet at a three-dimensional null point when its spines are torn apart.

The studied event was selected from the *TRACE* flare catalog.[5] *TRACE* is a NASA mission of the Small Explorer program, *SOHO* is a mission of International Cooperation between ESA and NASA. Our MHD calculations were done on the dual-core quadri-Opteron computers of the Service Informatique de l'Observatoire de Paris (SIO). The work of S.M. is funded by a fellowship of Direction Générale à l'Armement (DGA). The work of E.P. was supported, in part, by the NASA HTP and SR&T programs. Financial support by the European Commission through the SOLAIRE Network (MTRN-CT-2006-035484) is gratefully acknowledged.

APPENDIX

VORTICITY DRIVEN CURRENT SHEET FORMATION AND RECONNECTION TRIGGERING IN NULL-POINT GEOMETRY

In Section 5, we have mentioned that the perturbations originating from distant regions, away from the three-dimensional null point, do not only lead to compressive motions around the null point. Following Litvinenko (2006), we argue that incompressible shearing motions lead to the development of a vorticity sheet that is at the origin of a current sheet in viscous and nonresistive MHD. We further propose that it leads to its subsequent pinching and therefore to the increase of the current intensity and to efficient magnetic reconnection at the null. In the following, we address these hypotheses with a simple analytical 2.5D model, where $(\mathbf{e}_x, \mathbf{e}_y, \mathbf{e}_z)$ are the orthogonal unit vectors of a Cartesian domain where z is the axis of invariance.

Let us consider a potential two-dimensional null point, which divergence free and irrotational magnetic field is given by

$$\mathbf{b}(t=0) = B_0 \begin{pmatrix} x \\ -y \\ 0 \end{pmatrix} \tag{A1}$$

where B_0 is a constant. Even though three-dimensional fans and spines cannot be strictly defined in such a model, let us assume, for the sake of the argument, that the spine (resp. fan) field lines are those aligned with the y (resp. x-axis), and originating from

[5] http://hea-www.harvard.edu/trace/flare_catalog/cflares.html

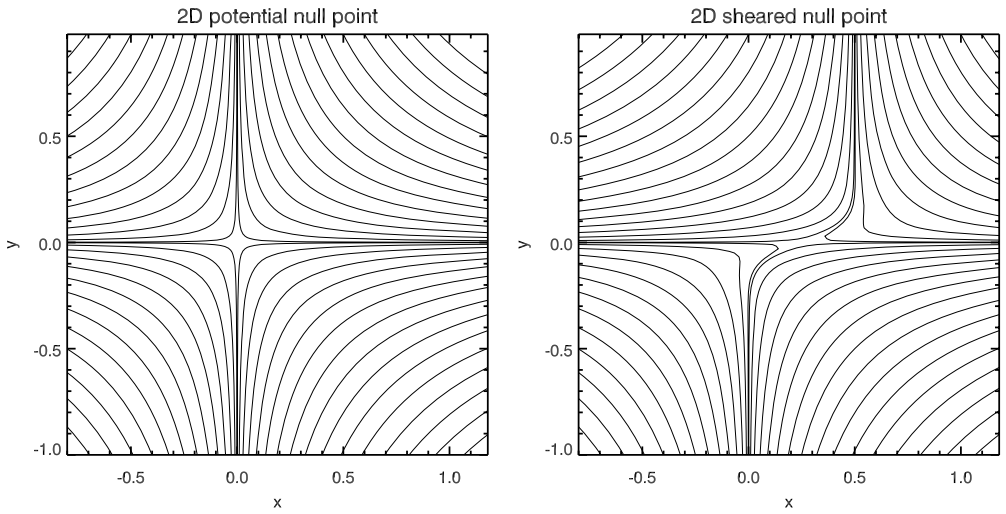

Figure A1. Field lines in the two-dimensional null-point model, in the potential field case $\mathbf{b}(t=0)$ (left panel) and in the sheared case $\mathbf{b}(t)$ (right panel) for $U_0 t = 0.5$ and $e = 0.1$ (see the text). The field lines are the same in both panels, i.e., they are the same isocontours of the potentials Φ_0 and Φ_t.

the null point at (0, 0, 0). A potential Φ can be associated with any 2.5D magnetic field, as defined by

$$\mathbf{b} = \nabla\Phi \times \mathbf{e}_z + b_z \mathbf{e}_z. \tag{A2}$$

At $t = 0$, the expression Φ_0 of this potential for $\mathbf{b}$ is

$$\Phi_0 = B_0 xy. \tag{A3}$$

Magnetic field lines are then readily given by isocontours of this potential (see Figure A1, left panel).

By analogy to what happens in our three-dimensional MHD simulation, let us consider a simple kinematic incompressible shearing motion along x that can be applied for the upper spine, while leaving the lower spine unchanged:

$$\mathbf{u} = \frac{U_0}{2}\begin{pmatrix} 1+\tanh(y/e) \\ 0 \\ 0 \end{pmatrix}. \tag{A4}$$

The velocity magnitude along x for $y \gg 0$ is U_0 and e is the finite half-width of the layer located around $y = 0$ between the shearing motions above the fan and the nonmoving regions below it. Such a finite scale naturally comes from viscous effects, which are always finite in real plasmas, and which are much larger than the resistivity in the solar corona (Litvinenko 2006). This shearing flow results in a vorticity ω, given by

$$\omega = \nabla \times \mathbf{u} = -\frac{U_0}{2e}\cosh^{-2}\left(\frac{y}{e}\right)\mathbf{e}_z. \tag{A5}$$

By construction, the vorticity is therefore nonnull only along z and confined to the $|y| \lesssim e$ domain.

The ideal MHD induction equation has to be solved to calculate the magnetic field which results from the shearing motion. It shows that only b_x evolves in time:

$$\frac{\partial \mathbf{b}}{\partial t} = \nabla \times (\mathbf{u} \times \mathbf{b}) = \begin{pmatrix} -B_0(u_x - y\omega_z) \\ 0 \\ 0 \end{pmatrix}. \tag{A6}$$

The solution for the magnetic field at any time t with this partial differential equation is $\mathbf{b}(t) = (b_x(t=0) - B_0 t(u_x - y\omega_z))\mathbf{e}_x + b_y(t=0)\mathbf{e}_y$, hence

$$\mathbf{b}(t) = B_0 \begin{pmatrix} x - (U_0 t/2)[1 + \tanh(y/e) + (y/e)\cosh^{-2}(y/e)] \\ -y \\ 0 \end{pmatrix}. \tag{A7}$$

The corresponding potential Φ_t given by Equation (A2) is

$$\Phi_t = B_0 y\left[x - \frac{U_0 t}{2}\left(1 + \tanh\left(\frac{y}{e}\right)\right)\right]. \tag{A8}$$

The resulting field lines for $\mathbf{b}(t)$ are drawn in Figure A1 (right panel) for $U_0 t = 0.5$ and $e = 0.1$. The upper half of the configuration has uniformly slid along the fan along x, while the field lines have been differentially sheared for $|y| \lesssim e$. Interestingly, the effect of the finite viscosity results in a configuration that looks like it is reconnecting (even though it is not), since some field lines have very pronounced kinks for $x \in [0, 0.5]$ in the region $|y| \leqslant e$. In terms of field lines, this two-dimensional model is very similar to the results of our three-dimensional MHD calculations (see Figure 5) as well as some others studies (e.g., Pontin et al. 2007a; Pariat et al. 2009): the upper and lower spines are not facing each other any more.

Calculating the electric current density from $\mathbf{j} = \mu^{-1}\nabla \times \mathbf{b}$, one finds that the current only flows along z and is given by

$$\mathbf{j} = \left(2B_0 t\frac{\partial u_x}{\partial y} + yB_0 t\frac{\partial^2 u_x}{\partial y^2}\right)\mathbf{e}_z \tag{A9}$$

$$= \frac{B_0 U_0 t}{\mu_0 e}\cosh^{-2}\left(\frac{y}{e}\right)\left[1 - \frac{y}{e}\tanh\left(\frac{y}{e}\right)\right]\mathbf{e}_z. \tag{A10}$$

One immediately sees that this simple model creates a current density that does not vary with x, so it has equal magnitudes around the null point in between both spines, and far from this region along the spine. This uniform current density along the fan is not recovered in the MHD models, however we discuss hereafter how this apparent artifact should not remain if one lets this configuration relax. In the simple model, the sign of the currents depend on the amplitude of the term $\zeta = (y/e)\tanh(y/e)$. Close to the fan, for $|y| \ll e$, $\zeta \leqslant 1$

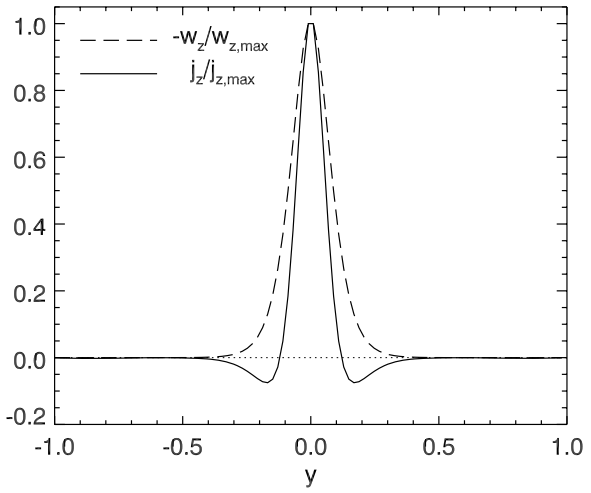

Figure A2. Plots of the normalized current density j_z (solid line) and vorticity ω_z (dashed line) along the y-axis for the sheared field $\mathbf{b}(t)$.

and $j_z \simeq -(2B_0t/\mu_0)\omega_z \propto \omega_z$. For $|y| \gg e$, the $\cosh^{-2}(y/e)$ factor results in negligible currents, so that the magnetic field is there nearly potential. For $|y| \gtrsim e$, then $\zeta \leqslant 1$ and the current changes its sign but its magnitude remains well below its intensity in the vicinity of the fan, due to the $\cosh^{-2}(y/e)$ factor. Figure A2 illustrates this analysis, displaying an overlay of $j_z(y)$ and $-\omega_z(y)$.

One can now discuss the fate of such a configuration if the system is relaxed from its kinematic constraint, and is allowed to evolve under the full MHD equations. To do so, one can calculate the Lorentz force in $\mathbf{b}(t)$, given by the usual expression $\mathbf{F}_L = \mathbf{j} \times \mathbf{b}$, one obtains

$$\mathbf{F}_L = F_0 \begin{pmatrix} y \\ x - (U_0t/2)[1 + \tanh(y/e) + (y/e)\cosh^{-2}(y/e)] \\ 0 \end{pmatrix}, \tag{A11}$$

$$\text{with} \quad F_0 = \frac{B_0^2 U_0 t}{e} \cosh^{-2}\left(\frac{y}{e}\right)\left[1 - \frac{y}{e}\tanh\left(\frac{y}{e}\right)\right]. \tag{A12}$$

This expression being quite challenging, even though we performed an analytical analysis, hereafter we present a graphical analysis, based on a typical configuration plotted in Figure A3 : here some vectors of the Lorentz force are plotted for $U_0t = 0.5$ and $e = 0.1$. First, in the area which surrounds the teared null point, for $x \in [0.1, 0.4]$, $F_L(y)$ switches the direction across the fan. So the forces will induce there a pinching of the current sheet. This pinching could enhance reconnection, if the vorticity sheet has developed on a scale length larger than (or comparable to) the resistive scale, depending on the viscosity. A large-enough initial shearing of the configuration could there produce Lorentz forces of large magnitudes, which could overcome the pressure gradients that would develop in this layer to counteract the pinching. Second, in the two regions located further away from the null point, where the spines have been differentially sheared, the kink in the field lines result in strong magnetic tension forces pointing away from the null point. The resulting motions would tend to facilitate the pinching and therefore the reconnection by accelerating away the material previously advected toward the null. Third, in the areas surrounding the fan

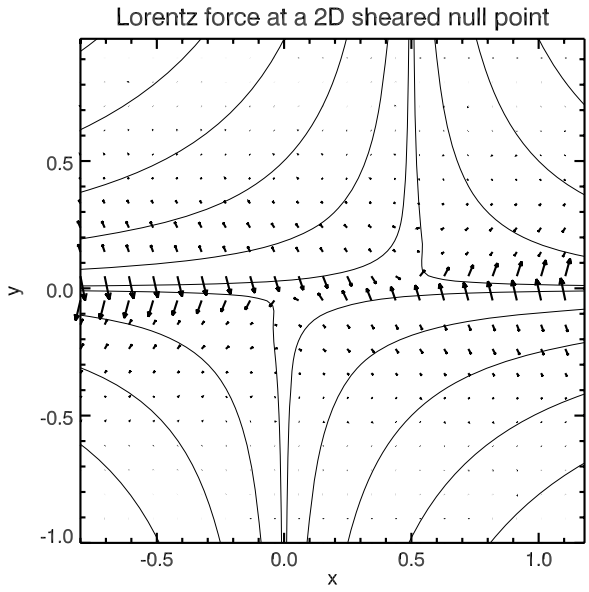

Figure A3. Selection of field lines in the sheared model $\mathbf{b}(t)$, overplotted with a Lorentz force $\mathbf{F}_L$ vectors indicated by short thick arrows.

for $x \leqslant -0.2$ and $x \geqslant 0.7$, $F_L(y)$ only points downward and upward, respectively. Assuming that the line-tied (photospheric) boundary is located at distances $|x| \gg 1$, we argue that these forces would launch Alfvén waves, which would take away the corresponding stress farther and farther from the null-point area. This would greatly reduce the current density in the fan in these regions, only leaving the reconnecting current sheet around the null point itself.

In summary, we have demonstrated that: (1) the vorticity sheet, which results from the shearing motion, naturally produces a co-spatial current sheet, of a slightly smaller width; (2) intense currents will eventually only remain around the null point, along the fan, between the teared spines; (3) the shearing motion prescribed parallel to the fan, will induce pinching motions nearly perpendicular to the fan, and eventually enhance magnetic reconnection at the null point.

REFERENCES

Alissandrakis, C. E. 1981, A&A, 100, 197
Antiochos, S. K. 1996, in ASP Conf. Ser. 95, Solar Drivers of the Interplanetary and Terrestrial Disturbances, ed. K. S. Balasubramaniam, S. L. Keil, & R. N. Smartt (San Francisco, CA: ASP), 1
Antiochos, S. K., Karpen, J. T., & DeVore, C. R. 2002, ApJ, 575, 578
Aulanier, G., DeLuca, E. E., Antiochos, S. K., McMullen, R. A., & Golub, L. 2000, ApJ, 540, 1126
Aulanier, G., Démoulin, P., & Grappin, R. 2005a, A&A, 430, 1067
Aulanier, G., Pariat, E., & Démoulin, P. 2005b, A&A, 444, 961
Aulanier, G., et al. 2007, Science, 318, 1588
Aulanier, G., Pariat, E., Démoulin, P., & Devore, C. R. 2006, Sol. Phys., 238, 347
Bogachev, S. A., Somov, B. V., Kosugi, T., & Sakao, T. 2005, ApJ, 630, 561
Démoulin, P., Bagala, L. G., Mandrini, C. H., Henoux, J. C., & Rovira, M. G. 1997, A&A, 325, 305
Démoulin, P., Henoux, J. C., & Mandrini, C. H. 1994a, A&A, 285, 1023
Démoulin, P., Mandrini, C. H., Rovira, M. G., Henoux, J. C., & Machado, M. E. 1994b, Sol. Phys., 150, 221
Démoulin, P., Henoux, J. C., Priest, E. R., & Mandrini, C. H. 1996, A&A, 308, 643
Fletcher, L., & Hudson, H. 2001, Sol. Phys., 204, 69
Fletcher, L., Metcalf, T. R., Alexander, D., Brown, D. S., & Ryder, L. A. 2001, ApJ, 554, 451
Fletcher, L., Pollock, J. A., & Potts, H. E. 2004, Sol. Phys., 222, 279
Galsgaard, K., & Nordlund, Å. 1997, J. Geophys. Res., 102, 231
Galsgaard, K., Priest, E. R., & Titov, V. S. 2003, J. Geophys. Res. (Space Physics), 108, 1042

Georgoulis, M. K., Rust, D. M., Bernasconi, P. N., & Schmieder, B. 2002, ApJ, 575, 506
Gorbachev, V. S., Kelner, S. R., Somov, B. V., & Shvarts, A. S. 1988, Sov. Astron., 32, 308
Gorbachev, V. S., & Somov, B. V. 1989, Sov. Astron., 33, 57
Grappin, R., Aulanier, G., & Pinto, R. 2008, A&A, 490, 353
Grigis, P. C., & Benz, A. O. 2005, ApJ, 625, L143
Handy, B. N., et al. 1999, Sol. Phys., 187, 229
Heyvaerts, J., Priest, E. R., & Rust, D. M. 1977, ApJ, 216, 123
Hornig, G., & Priest, E. 2003, Phys. Plasmas, 10, 2712
Krucker, S., Fivian, M. D., & Lin, R. P. 2005, Adv. Space Res., 35, 1707
Krucker, S., Hurford, G. J., & Lin, R. P. 2003, ApJ, 595, L103
Lau, Y.-T., & Finn, J. M. 1990, ApJ, 350, 672
Lin, J. 2004, Sol. Phys., 222, 115
Litvinenko, Y. E. 2006, Phys. Plasmas, 13, 092305
Longcope, D. W. 2005, Living Rev. Solar Phys., 2, 7
Mandrini, C. H., Démoulin, P., Bagala, L. G., van Driel-Gesztelyi, L., Henoux, J. C., Schmieder, B., & Rovira, M. G. 1997, Sol. Phys., 174, 229
Mandrini, C. H., Démoulin, P., Henoux, J. C., & Machado, M. E. 1991, A&A, 250, 541
Mandrini, C. H., Démoulin, P., Rovira, M. G., de La Beaujardiere, J.-F., & Henoux, J. C. 1995, A&A, 303, 927
Manoharan, P. K., & Kundu, M. R. 2003, ApJ, 592, 597
Mellor, C., Titov, V. S., & Priest, E. R. 2003, Geophys. Astrophys. Fluid Dyn., 97, 489
Moore, R. L., Sterling, A. C., Hudson, H. S., & Lemen, J. R. 2001, ApJ, 552, 833
Pariat, E., Antiochos, S. K., & DeVore, C. R. 2009, ApJ, 691, 61
Pariat, E., Aulanier, G., Schmieder, B., Georgoulis, M. K., Rust, D. M., & Bernasconi, P. N. 2004, ApJ, 614, 1099
Pariat, E., Schmieder, B., Berlicki, A., Deng, Y., Mein, N., López Ariste, A., & Wang, S. 2007, A&A, 473, 279
Parnell, C. E., Neukirch, T., Smith, J. M., & Priest, E. R. 1997, Geophys. Astrophys. Fluid Dyn., 84, 245
Parnell, C. E., Smith, J. M., Neukirch, T., & Priest, E. R. 1996, Phys. Plasmas, 3, 759
Pneuman, G. W. 1981, in Solar Flare Magnetohydrodynamics (New York: Gordon and Breach Science), 379
Pontin, D. I., Bhattacharjee, A., & Galsgaard, K. 2007a, Phys. Plasmas, 14, 052106
Pontin, D. I., Bhattacharjee, A., & Galsgaard, K. 2007b, Phys. Plasmas, 14, 052109
Pontin, D. I., & Galsgaard, K. 2007, J. Geophys. Res. , 112, 3103
Pontin, D. I., Hornig, G., & Priest, E. R. 2004, Geophys. Astrophys. Fluid Dyn., 98, 407
Pontin, D. I., Hornig, G., & Priest, E. R. 2005, Geophys. Astrophys. Fluid Dyn., 99, 77
Priest, E. R., & Démoulin, P. 1995, J. Geophys. Res., 100, 23443
Priest, E. R., & Forbes, T. G. 1992, J. Geophys. Res., 97, 1521
Priest, E. R., & Forbes, T. G. 2002, A&A Rev., 10, 313
Priest, E. R., Hornig, G., & Pontin, D. I. 2003, J. Geophys. Res., 108, 1285
Priest, E. R., & Titov, V. S. 1996, Phil. Trans. R. Soc. Lond. A, 354, 2951
Qiu, J. 2009, ApJ, 692, 1110
Rickard, G. J., & Titov, V. S. 1996, ApJ, 472, 840
Scherrer, P. H., et al. (& MDI Engineering Team) 1995, Sol. Phys., 162, 129
Schmieder, B., Forbes, T. G., Malherbe, J. M., & Machado, M. E. 1987, ApJ, 317, 956
Schmieder, B., & Pariat, E. 2007, Scholarpedia, 2, 4335
Schrijver, C. J. 2009, Adv. Space Res., 43, 739
Schrijver, C. J., DeRosa, M. L., Title, A. M., & Metcalf, T. R. 2005, ApJ, 628, 501
Schrijver, C. J., & Title, A. M. 2002, Sol. Phys., 207, 223
Sturrock, P. A. 1968, in IAU Symp. 35, Structure and Development of Solar Active Regions, ed. K. O. Kiepenheuer (Dordrecht: Kluwer), 471
Titov, V. S., Hornig, G., & Démoulin, P. 2002, J. Geophys. Res., 107, 1164
Titov, V. S., Priest, E. R., & Démoulin, P. 1993, A&A, 276, 564
Ugarte-Urra, I., Warren, H. P., & Winebarger, A. R. 2007, ApJ, 662, 1293
van Driel-Gesztelyi, L., Hofmann, A., Démoulin, P., Schmieder, B., & Csepura, G. 1994, Sol. Phys., 149, 309